2023 International Ocean Energy Symposium & 20th Joint Young Research Forum

Date	**September 15-16, 2023**
Venue	**Industry-Academic Hub Hall (G2, 201), KMOU**
Participation	**Korea Maritime & Ocean University (KMOU, Korea)** **Pukyong National University (PKNU, Korea)** **Mokpo National Maritime University (MMU, Korea)** **Mokpo National University (MNU, Korea)** **Saga University (SAGA-U, Japan)** **National Fisheries University (NFU, Japan)**
Sponsor	**Graduate School & Department of Green and Smart Ship Equipment (KMOU)**

CONTENTS

Poster Presentation

2023 International Ocean Energy Symposium & 20th Joint Young Research Forum

Words for invitation

This symposium is held every year between Korea and Japan University every other year.

This symposium topics of interest include technology of ocean energy. And this symposium is aimed at promoting cooperation not only among professors and researchers but also between all experts in the ocean energy technology field.

This symposium will provide various programs, such as academic paper presentations, poster sessions, invited talks and also some other activities for promoting cooperative relation.

We sincerely wish to have your interest and participation that will make this forum a success.

Sincerely yours,

Organizer:

Ph.D *Cheol OH*, Ph.D *Sung-Hwan YOUN*, Ph.D Jun-Seong KIM

Program

September 15 (Fri.)

Time	Event	Remark
09:30 - 10:00	Registration	Participant
10:00 – 10:15	Greetings	
10:15 – 12:00	Oral Presentation (1)	Presenters: 7
12:00 – 14:00	Lunch time	
14:00 – 15:00	Poster Presentation	Presenters: 8
15:00 – 17:00	Oral Presentation (2)	Presenters: 7
17:00 – 18:00	Go to dinner	
18:00 – 20:00	Welcome dinner	

September 16 (Sat.)

Time	Event	Remark
09:00 - 13:00	Meeting	

◎ Oral Presentation (1)

Chairman: Jun-Seong KIM (KMOU)

10:15~10:30	An Experimental Observation on Thermal Runaway of 18650 Lithium-Ion Battery	*Ju-Won PARK*	*KMOU*
10:30~10:45	Study on Evaluation of Heat Transfer Performance of Heat Exchanger in Hybrid Cycle of Ocean Thermal Energy Conversion	*Tomohide NISHIMURA*	*SAGA-U*
10:45~11:00	Fabrication of a Heat Exchanger for Two-Phase Flow in Organic Rankine Cycle System for Ships	*Dae-Jung HWANG*	*KMOU*
11:00~11:15	Experimental Study of Marine Biofouling for the Plate Type Heat Exchanger with Seawater Cooling -Efficacy of Electromagnetic Processing Equipment	*Naoki KIYAMA*	*NFU*
11:15~11:30	N_2O Decomposition and Kinetic Modeling with Varying Reaction Temperatures and Residence Times	*Su-Hyeon KIM*	*KMOU*
11:30~11:45	Posture Control of Counter-rotating Propeller Type Tidal Power Unit with Winglet	*Haruto FUCHIWAKI*	*SAGA-U*
11:45~12:00	A Study on Performance Improvement of Boil-off Gas Re-liquefaction Systems for LNG-fueled Ships	*Jun-Seong KIM*	*KMOU*

◎ Oral Presentation (2)

Chairman: Yasutaka IMAI (SAGA-U)

15:00~15:15	Flame Surfaces Variation through Ionic Wind and Flame Stretch in Mass-Diffusively Unstable Flame	*Si-Yeong YU*	*KMOU*
15:15~15:30	Research on buoy shape to improve wave energy conversion efficiency	*Takuma IMAIZUMI*	*SAGA-U*
15:30~15:45	Correlation between Ionic Wind and Thermo-Acoustic Instability in Downward-Propagating Premixed Flame under Electric	*Dae-Won IM*	*KMOU*
15:45~16:00	Study of Power Generation System Utilizing Waste Heat from Marine Engine (Possibility of introducing HFO Refrigerant)	*Atsuyoshi ETSUKAWA*	*NFU*
16:00~16:15	*Break*		
16:15~16:30	Combustion field measurement of temperature, concentration and velocity using TDLAS	*Jeong-Woong HONG*	*KMOU*
16:30~16:45	Tip clearance gap effect on the hydraulic performance of a mixed flow pump with semi-open casing	*Ujjwal SHRESTHA*	*MNU*
16:45~17:00	A study of fuel cell-battery propulsion system for four types of vessels	*Jong-In Kim*	*KMOU*

◎ Poster Presentation

Chairman: Junichi OHARA (NFU)

Characteristics of HFO Refrigerants in Double-Stage Reverse Rankine Cycle Refrigerator	*Tetsuya HONDA*	*NFU*
Oceanographic Survey for Installation of OTEC Plant in Kumejima Island (Influence from the Aguni Basin)	*Shodai NAGATA*	*NFU*
Research on Periodic Characteristics by Visualization of Plate Type Evaporator Interior	*Ayano NAKAGAWA*	*SAGA-U*
Development of Optimization Method of Jacket Structures of Offshore Wind Turbines	*Takahiro NAGATSU*	*SAGA-U*
Heat transfer characteristics of FCU and plate heat exchanger in seawater air conditioning system	*Haruki IDA*	*SAGA-U*
Boiling heat transfer characteristics of ammonia in micro channel and plate heat exchanger	*Shoichi SUEHIRO*	*SAGA-U*
Research on optimal design of ocean thermal energy conversion system	*Takayuki HARAGUCHI*	*SAGA-U*
Research on hot spring water power generation using hybrid cycle	*Tomoyuki HIRAISHI*	*SAGA-U*

ORAL

PRESENTATION

An Experimental Observation on Thermal Runaway of 18650 Lithium-Ion Battery

Juwon Park[1,2)], Daegeun Park[3)] and Sung Hwan Yoon[1,2)]

Department of Marine System Engineering, Korea Maritime and Ocean University, 727 Taejong-ro, Yeongdo-gu, Busan, 49112, Republic of Korea[1)]
Interdisciplinary Major of Maritime AI Convergence, Korea Maritime and Ocean University, 727 Taejong-ro, Yeongdo-gu, Busan, 49112, Republic of Korea[2)]
Carbon Neutral Technology R&D Department, Korea Institute of Industrial Technology (KITECH), 89 Yangdaegiro-gil, Seobuk-gu, Cheonan, 31056, Republic of Korea[3)]

The need for a 'Rechargeable battery' is growing as a driving force in the information and communication device and electric vehicle industry. Unlike disposable primary cell, rechargeable battery that can be semi-permanently reused through charging after discharging is a device that store external electrical energy after converting external electrical energy into chemical energy form and make electric energy when necessary.

For about 120 years, rechargeable batteries have been useful in everyday life in various forms, such as lead-acid batteries, nickel-cadmium batteries, nickel-hydrogen batteries, etc. Among them, a lithium-ion battery, which can be used for a long time without frequent charging, is currently used as a typical rechargeable battery. Lithium-ion battery has an advantage of high energy density and excellent power, and have a long life due to no memory effect. Therefore, lithium-ion battery is used in various fields such as laptops, mobile phones, drones, and electric vehicles. In particular, in the case of electric vehicle that uses a lithium-ion battery as the main power, the 2021 Global Electric Vehicle Outlook Report released by the International Energy Agency (IEA) reported that the share of electric vehicle in the global automobile market will soar to 12% by 2030.

However, the issue of safety is constantly being raised due to the thermal runaway that could occur due to internal or external factors of a lithium-ion battery. Thermal runaway has been reported to rapidly burn and explode due to mechanical, electrical, and thermal defects[1-3)]. If a thermal runaway occurs in the battery pack, adjacent cells also cause a thermal runaway due to the generation of very high heat. As a lithium-ion battery has large internal energy, it is very difficult to suppress the thermal runaway once generated.

Therefore, a suppression study on the thermal runaway phenomenon is essential by experimentally observing the mechanism for the thermal runaway phenomenon.

The purpose of this study is to experimentally observe the mechanism for the thermal runaway of a lithium-ion battery and propose a technology to suppress the thermal runaway. Thermal runaway of the lithium-ion battery was observed by adjusting the supplied heat transfer coefficient and SOC level, and an inert gas was formed in a chamber to suppress the thermal runaway. As a result, if the internal temperature of the lithium-ion battery increased, it was determined that a thermal runaway caused by the internal defect of the lithium-ion battery would inevitably occur. The lithium-ion battery consists of cathode material, anode material, separator, and electrolyte, but if the structure of the separator is damaged due to internal or external defects, the chemical reaction caused by the short circuit between the cathode material and anode material causes a thermal runaway. However, it is observed that thermal runaway is suppressed because of the reduction of internal energy if the SOC-level is below 80% in this study, through this study, we will discuss how to quickly extinguish a fire caused by thermal runaway even if thermal runaway occurs.

References

(1) Wang, Q., et al., "A Review of Lithium Ion Battery Failure Mechanisms and Fire Prevention Strategies." Combust. Sci., 2019, 73, pp. 95-131.
(2) Zhong, G., et al., "Experimental Analysis of Thermal Runaway Propagation Risk within 18650 Lithium-Ion Battery Modules." J. Electrochem. Soc., 2018, 165, pp. A1925-A1934.
(3) Baird, A.R., et al., "Explosion Hazards from Lithium-Ion Battery Vent Gas." J. Power Sources, 2020, 446, pp.1-13.

・**Title**

「Study on Evaluation of Heat Transfer Performance of Heat Exchanger in Hybrid Cycle of Ocean Thermal Energy Conversion」

・Authors

Yasuyuki Ikegami (Saga Univ.)　Takeshi Yasunaga (Saga Univ.)
Takafumi Morisaki (Saga Univ.)　Shuji Miyazono (Saga Univ.)
Yoshitaka Otakara (Saga Univ.)　Tomohide Nishimura (Saga Univ.)

・Abstract

Ocean Thermal Energy Conversion (OTEC) is a type of power generation that utilizes the temperature difference between the surface and deep layers of the ocean and is attracting attention as a form of renewable energy. However, because OTEC directly passes seawater, which is the heat source, through an evaporator, it is necessary to use a heat exchanger made of titanium, which is expensive due to the deterioration of the heat transfer performance of the heat exchanger in the evaporator caused by contamination from marine organisms and the corrosion of seawater. To solve this problem, a hybrid cycle OTEC (H-OTEC) was proposed.

H-OTEC combines a seawater desalination system with OTEC. The evaporator in H-OTEC is called an evaporator-condenser (Eva-Con) because it condenses the heat source at the same time. The Eva-Con is also a particularly important piece of equipment because it connects the power generation system to the desalination system. My objective was to experimentally evaluate the heat transfer performance of the Eva-Con by conducting performance tests. Furthermore, I aimed to calculate experimental equations for the heat transfer coefficients of both the heat source and the working fluid (Ammonia) of the Eva-Con.

・Structure of the paper

Fabrication of a Heat Exchanger for Two-Phase Flow in Organic Rankine Cycle System for Ships

Dae Jung Hwang[1] · Tae Woo Lim[2] · Jae Hoon Jee[3] · Eun Shin Bang[4] · Cheol Oh†

Unlike conventional heat exchangers, a meticulous design approach is required for Waste Heat Recovery Units (WHRU) and condensers utilized in Organic Rankine Cycle (ORC) power systems. This is due to incorporating phase change phenomena and utilizing a refrigerant as a working fluid instead of water. The purpose of this study is to fabricate a waste heat recovery unit and condenser that are capable of operating stably and efficiently for the use of ORC systems in ships.

In this study, WHRU and Condenser were designed using numerical analysis techniques, and prototypes were fabricated based on these designs. In addition, the validity of the heat exchanger CFD modeling was confirmed through comparison of the simulation results with those obtained from the prototype's experimental testing. The starting position of phase change, a crucial factor for stable operation in terms of two-phase flow, was predicted for each refrigerant when an actual heat exchanger was employed in a ship.

The WHRU experiment confirmed a heat transfer rate of 403 ㎾ and a phase change, where the refrigerant changed from a liquid state at an inlet temperature 31℃ to a superheated vapor state 78℃ upon discharge. As a result of the experiment of the condenser, it has been confirmed that there is a heat transfer rate of 113 ㎾ and a phase change occurs when a refrigerant, in a gaseous state at a temperature of 74℃, is introduced at the inlet and discharged in a supercooled state at 38℃.

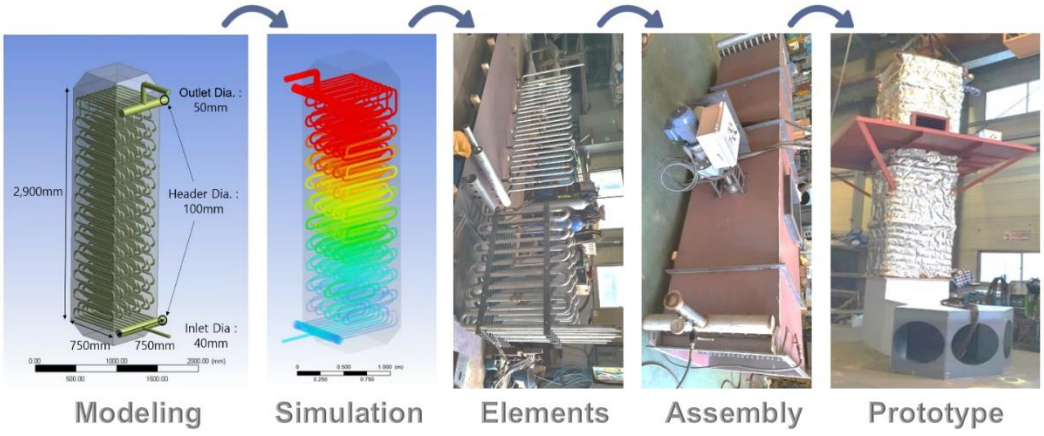

Fig. 1 Process of design and fabrication of WHRU

† Corresponding Author: Professor, Division of Marine System Engineering, Korea Maritime & Ocean University, E-mail: ohcheol@kmou.ac.kr

1 Researcher, Department of Marine Environment, Korea Maritime Cooperation Center, E-mail: hdaejung@imkmc.or.kr

2 Professor, Division of Marine System Engineering, Korea Maritime & Ocean University, E-mail: kyunlim@kmou.ac.kr

3 Professor, Division of Maritime Police, Mokpo National Maritime University, E-mail: jhjee@mmu.ac.kr

4 Ph. D., Division of Marine System Engineering, Korea Maritime & Ocean University, E-mail: esbang627@kmou.ac.kr

Experimental Study of Marine Biofouling for the Plate Type Heat Exchanger with Seawater Cooling -Efficacy of Electromagnetic Processing Equipment

Naoki KIYAMA[1)], Junichi OHARA[1)], Hideyuki YOSHIMURA[1)], Masaki ARIYOSHI[1)], Syuhei KUGIMIYA[1)], Minoru MATSUSHITA[2)] and Yasuyuki IKEGAMI,[3)]

National Fisheries University, 2-7-1 Nagatahonmachi, Shimonoseki-shi, Yamaguchi 759-6595, Japan [1)]
Hisaka Corporation, 2-1-48 Higashikonoikechou, Higashiosaka-shi, Osaka 578-0973, Japan [2)]
Institute of Ocean Thermal Energy, Saga University, 1-Honjomachi, Saga-shi, Saga 840-8502, Japan[3)]

Abstract

In this study, the antifouling effect of the electromagnetic processing equipment on seawater was verified by conducting long-term experiments using the electromagnetic processing equipment, which is an antifouling device, to reduce fouling of the heat transfer surface on the seawater side of a plate heat exchanger with continuous seawater flow. The operation of the electromagnetic processing equipment in the seawater system of the plate heat exchanger for 90 days improved the rate of decrease of the heat transfer coefficient by 7.4% and the increase of the fouling factor by 32.5%. These results proved that the installation of an electromagnetic processing equipment in a plate heat exchanger has an antifouling effect against seawater fouling.

Key Words: Electromagnetic Processing Equipment , Plate Heat Exchanger , Fouling Factor

1. Introduction

Currently, the shipping industry is trying to reduce operating costs by introducing various technologies in response to soaring fuel prices. Plate heat exchangers, which are important equipment on ships, often utilize seawater and incur large maintenance costs.

Therefore, in this study, the antifouling effect of the electromagnetic processing equipment in seawater tube was verified by conducting long-term experiments. The equipment is an antifouling device to reduce fouling, which seawater continuously feeds on the seawater-side heat transfer surface.

2. Experimental Equipment

Figure 1 shows the schematic diagram of the experimental apparatus for seawater side contamination using a plate heat exchanger. The experimental apparatus consists of two plate heat exchangers, two seawater tanks (indoor and outdoor), a hot water tank, a cooling fan for the seawater tank (outdoor), a seawater pump, a hot water pump, a hot water circulation pump, two electromagnetic flow meters, and an electric water heater. The experiment was conducted with an electromagnetic processing equipment ZETAWAVE[1)] [Koshin Chemical Corporation, Technolab Co, Takashin Chemical Co.]. Installed plate heat exchangers are five [RX-015A-KNHJ-11, Hisaka Seisakusho], an effective total heat transfer area of 0.213 m^2, and three channels on the hot water and seawater sides, respectively. The electromagnetic processing equipment was installed in the No.1 test plate heat exchanger system, while the No.2 system was designed to have no effect of the electromagnetic processing equipment, so that comparisons can be made between the two systems with and without the electromagnetic processing equipment.

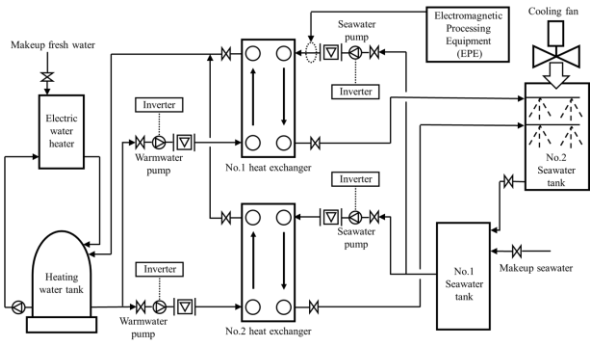

Fig.1 Diagrammatical view of the device

Table 1 Experimental conditions

Experimental conditions		
Electric water heater setting temperature	[℃]	40.0
Warm water inlet temperature	[℃]	40.0
Warm water flow rate	[L/s]	0.30
Sea water flow rate	[L/s]	0.30

3. Experimental Method and Conditions

Experimental data were measured for temperature, flow rate, and differential pressure, using a data lo gger at 12:00 AM. Experimental conditions are sho wn in Table 1. The experiment was conducted fro m April 9, 2023 to July 8, 2023, operating contin uously for 90 days.

4. Experimental Results

In this experiment, we verified the heat transfer coefficient, which indicates the performance of the plate heat exchanger, and the fouling factor, which evaluates the contamination of the plate surface, based on the results of the experiment. As reference data, the experimental results of the heat transfer coefficient and fouling factor for the case of an electromagnetic processing equipment conducted under the same conditions last year are also shown in the figure[2)]. The heat transfer coefficient and fouling factor for the case of an electromagnetic processing equipment are also shown in the figure.

4.1 Heat Transfer Coefficient

The heat transfer coefficient U is obtained from the following equation.

$$U = \frac{Q}{A\Delta T_m} \quad (1)$$

Figure 2 shows the change over time of the heat

transfer coefficient. Figure 2 shows that the heat transfer coefficient decreases continuously from the beginning of the experiment. After 90 days, the heat transfer coefficient decreased from 4418.7[W/(m^2-K)] to 2199.3[W/(m^2-K)] with the electromagnetic processing equipment, the decrease of 50.2%. Without the electromagnetic processing equipment, the heat transfer coefficient decreased from 4016.8 [W/(m^2-K)] to 1704.7 [W/(m^2-K)], the decrease of 57.6%. Therefore, it is clear that the electromagnetic processing equipment installed in the seawater system of the plate heat exchanger for 90 days can reduce the reduction of the heat transfer coefficient against seawater contamination by 7.4%

4.2 Fouling Factor

In actual heat exchangers, dirt adheres to the heat transfer surfaces during operation, degrading heat transfer performance. Although some guidelines have been proposed for the fouling factor, it is said to vary greatly depending on the nature of the fluid, temperature, flow velocity, etc. Here, we calculated the fouling factor under the experimental conditions and verified the effect of the electromagnetic processing equipment. In this experiment, the fouling factor R_{fre} was defined by the following equation

$$R_{fre} = \frac{1}{U_2} - \frac{1}{U_1} \quad (2)$$

Where U_1 is the heat transfer coefficient before fouling and U_2 is the heat transfer coefficient after fouling.

Figure 3 shows the change over time of the fouling factor. Figure 3 shows that the fouling factor has decreased continuously since the beginning of the experiment. After 90 days, the stain coefficient increased to 2.28×10^{-4}[m^2·K/W] with the electromagnetic processing equipment and to 3.38×10^{-4}[m^2·K/W] without the electromagnetic processing equipment. Therefore, it is clear that 32.5% antifouling effect against seawater fouling is possible by installing and operating an electromagnetic processing equipment in the seawater system of a plate heat exchanger for 90 days.

5. Conclusions

In this study, the antifouling effect of the electromagnetic processing equipment in seawater system was verified by conducting long-term experimentusing the electromagnetic processing equipment, which is an antifouling device, to reduce fouling of the heat transfer surface on the seawater side by continuously passing seawater through a plate heat exchanger, and the following results were obtained.

1) The rate of decrease in the heat transfer coefficient was improved by operating the plate heat exchanger with an electromagnetic processing equipment in the seawater system for 90 days, and it was found that the reduction in the heat transfer coefficient for 7.4% seawater contamination could be mitigated.
2) The increase in fouling factor was improved by operating the electromagnetic processing equipment in the seawater system of the plate heat exchanger for 90 days, and it was found that antifouling effectiveness against seawater fouling of 32.5% was possible.
3) The installation of an electromagnetic processing equipment in a plate heat exchanger proved to be effective in preventing seawater fouling.

References

(1) ZETAWAVE([Koshin Chemical Corporation, Te chnolab Co, Takashin Chemical Co.]) : https://www.koshin-chem.co.jp/20151211114446

(2) Kaede OKUSAKO : Study on the antifouling effect of plate heat exchangers on seawater - Verification of antifouling effect by long-term operation of electromagnetic processing equipment -. 2022 Graduation Thesis Presentation of the Department of Marine Machinery and Engineering, Fisheries University, Shimonoseki (2023).

(3) S.J.PUGH, G.F.HEWITT, H.MULLER-STEINHAGEN, “Fouling During the Use of Seawater as Coolant-the Development of a User Guide”, Heat Transfer Engineering, Vol. 26, No. 1 (2005), pp. 35-43.

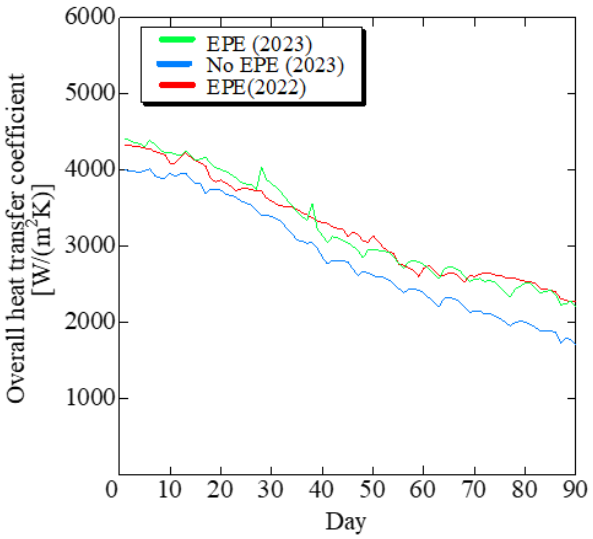

Fig. 2 Overall heat transfer coefficient with the day

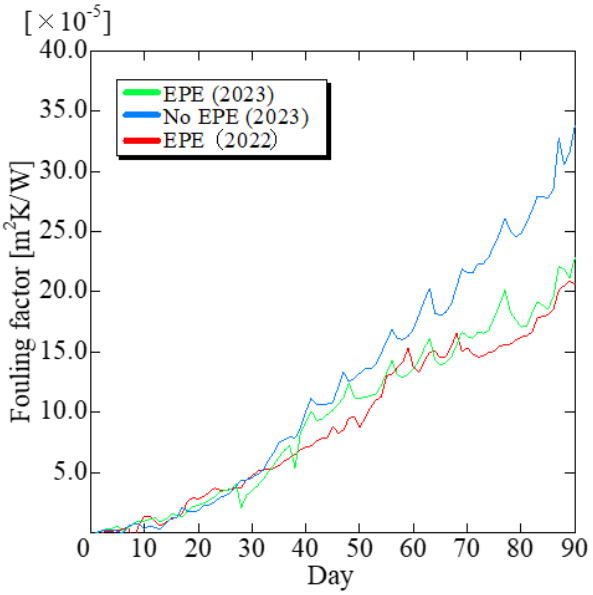

Fig. 3 The variation of fouling thermal resistance R_{fre} with the day

N_2O Decomposition and Kinetic Modeling with Varying Reaction Temperatures and Residence Times

Suhyeon Kim[1,2)], Daegeun Park[3)], Seung-Gon Kim[4)] and Sung Hwan Yoon[1,2)]

Department of Marine System Engineering, Korea Maritime and Ocean University, 727 Taejong-ro, Yeongdo-gu, Busan, 49112, Republic of Korea[1)]
Interdisciplinary Major of Maritime AI Convergence, Korea Maritime and Ocean University, 727 Taejong-ro, Yeongdo-gu, Busan, 49112, Republic of Korea[2)]
Carbon Neutral Technology R&D Department, Korea Institute of Industrial Technology (KITECH), 89 Yangdaegiro -gil, Seobuk-gu, Cheonan, 31056, Republic of Korea[2)]
Energy Efficiency Research Division, Korea Institute of Energy Research (KIER), 152 Gajeong-ro, Yuseong-gu, Daejeon, 34129, Republic of Korea[2)]

In July 2023, both Earth's surface temperature and sea surface temperature reached their highest recorded levels. If current greenhouse gas emissions persist, it's anticipated that all Arctic glaciers will completely melt by 2030[1)]. A NASA climate scientist cautioned, "Most people STILL underestimate the impending peril. This may well be the coolest summer for the rest of your life." Because even if global greenhouse gas reduction targets are met, it's anticipated that by 2050, all Arctic glaciers will vanish, even more substantial reductions in greenhouse gas emissions are needed than initially planned.

Within the maritime industry, significant efforts have been made to reduce greenhouse gas emissions through GHG (Greenhouse Gas) strategies. For carbon dioxide (CO_2) and methane(CH_4), technologies such as Carbon Capture, Utilization, and Storage (CCUS) and methane oxidation catalytic systems are employed for reduction. However, there is no significant progress on other greenhouse gases.

Nitrous oxide (N_2O), the third-largest emitted greenhouse gases, has a global warming potential approximately 300 times higher than CO_2 and produces NO and NO_2 in the stratosphere[2)]. Since these NOx emissions contribute to the gradual degradation of the ozone layer, it is imperative to reduce N_2O emissions.

N_2O is produced from sources such as fuel combustion in boilers and fossil fuel combustion. Notably, ammonia has recently received attention as a carbon substitute fuel, despite emitting significant amounts of NOx and N_2O during decomposition, thus necessitating technologies for their reduction.

This study focuses on decomposing high concentrations of N_2O under various reaction temperatures and residence times to determine the most efficient conditions. It also examines the pathways and concentrations of NOx generated during N_2O reduction. Additionally, we employed various rate constants to conduct numerical analysis using the Plug Flow Reactor (PFR), a 1D simulation model within Chemkin-Pro[3)]. Further details will be presented during an oral presentation[3)].

References

(1) Kim, Yeon-Hee. et al., "Observationally-constrained projections of an ice-free Arctic even under a low emission scenario." Nature Communications, 2023, 14.1, pp. 3139.
(2) Griggs, D.J., Noguer, M., “Climate Change 2001: The Scientific Basis. Contribution of Working Group I to The Third Assessment Report of The Intergovernmental Panel on Climate Change.” Weather 2002, 57, pp. 267-269.
(3) Kee, R.J., Rupley, F.M., Miller. J.A., “Chemkin-II: A Fortran Chemical Kinetics Package for The Analysis of Gas-phase Chemical Kinetics." Sandia National Lab.(SNL-CA), Livermore, CA (United States), 1989.

Posture Control of Counter-rotating Propeller Type Tidal Power Unit with Winglet

Haruto Fuchiwaki*, Tengen MURAKAMI** and Toshiaki KANEMOTO**
*Faculty of Science and Engineering, Saga University
1 Honjo, Saga 840-8502, Japan
E-mail: 22728014@edu.cc.saga-u.ac.jp
**Institute of Ocean Energy, Saga University
1 Honjo, Saga 840-8502, Japan

1. Introduction

The tidal current is expected as an attractive renewable energy source because the time change of flow direction and velocity is predictable. In this research, a mooring support structure is applied to the horizontal axis counter-rotating type power unit, which is not only save the initial cost due to the civil construction but also appropriate for using at narrow strait due to set up easily. The counter-rotating type power unit can keep the posture stable without rolling motion in the stream when it is mooring with a cable at moment center among the buoyancy, the gravity, and the drag force. In such an arrangement, the drag force induced from downstream type propellers works effectively to keep the horizontal posture. However, once the unit inclines against the mainstream by unexpected change of local flow velocity, the horizontal posture is disrupted and further aggravated by the drag force induced from the flow separation around the casing which includes a nacelle supporting a generator and two hubs of the front and rear propellers. Therefore, the winglet used in aircraft is set to the blade tip of the rear propeller to help the power unit recover to horizontal posture. In this study, the effects of winglet length on posture and blade performance were investigated by circulation type water channel tests and CFD.

2. Circulation type water channel tests

Fig. 1 shows the model power units with and without winglet at rear propeller. The length of winglets was varied in 3 cases (9 mm,19 mm,29 mm), and each ratio between length of winglet and the diameter of rear propeller are 0.038, 0.080, and 0.122. The generator is not installed in the models. The power unit consists of front propeller with three blades and rear propeller with five blades. The unit is set in a circulation type water channel with a cross-sectional area of 0.7 m (water depth) x 1.0 m (width) and moored with a wire at the nose spinner. In the experiments, the posture of the model was analyzed with the images by a camera. Besides, the rotational speeds of front and rear propeller were measured using a stroboscope (SATOTECH DT-2349JP). In the following discussion, the power unit model with winglet is called as PU_W in comparison with PU_O of the model without the winglet. The flow velocity V_{in} was changed from 0.7 m/s to 0.8 m/s, 0.9 m/s and 1.0 m/s.

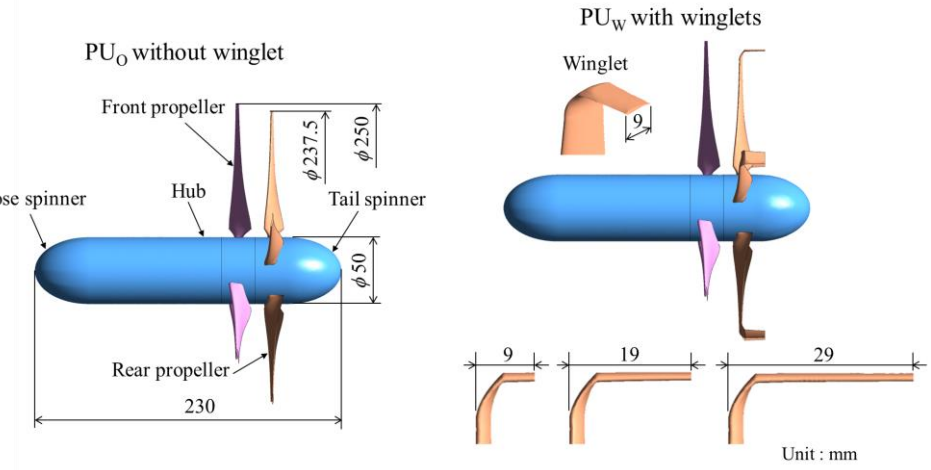

Fig. 1 Model units with and without winglet at rear propeller

Fig. 2 shows the tilt angle θ between horizontal direction and the axes of propellers. Besides, Fig. 3 is the counter-

rotational speed N_t. As shown in these figures, the tilt angle θ became low with increase of the winglet length. On the other hand, the counter-rotational speed N_t was higher in case $PU_{W0.080}$.

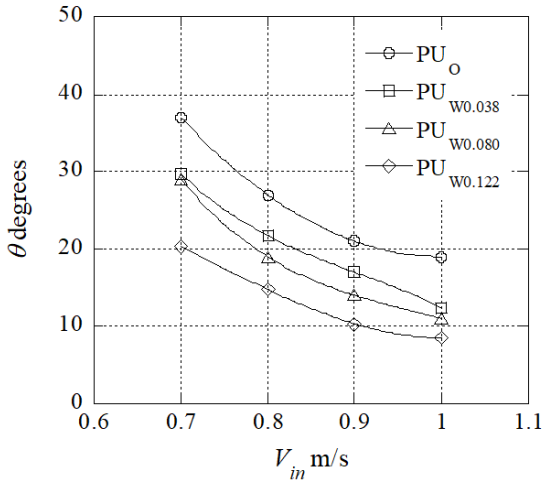

Fig. 2 Changes in tilt angle θ due to flow velocity V_{in}

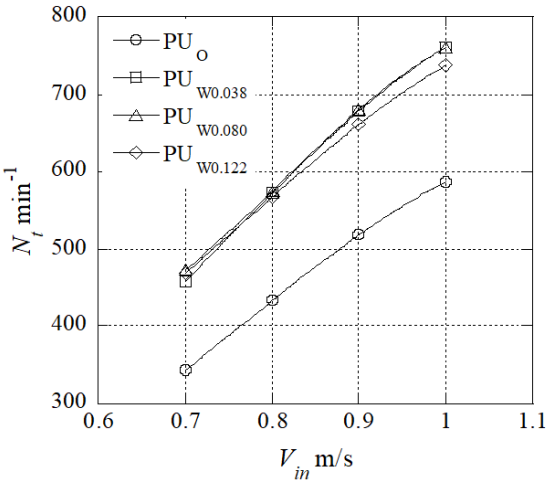

Fig. 3 Changes in counter-rotational speed N_t

3. Numerical simulations

The 3-D turbulent flow was simulated at the steady state condition by the commercial CFD code of ANSYS-CFX ver.19 with SST turbulent model to understand the propeller performances with and without winglet. The simulation domain is composed of 1 pitch passage areas of front and rear propellers. Fig. 4 is the changes in torque due to tip speed ratio λ and Fig. 5 shows the power coefficient C_p, where the λ is defined as the ratio of the circumferential velocity at blade tip and the flow velocity. The torque and the C_p were divided by ones at $\lambda = 6.4$ giving the maximum power coefficient C_p in case PU_O. As shown in Fig. 4 and Fig. 5, the torque and power coefficient C_p were higher in case $PU_{W0.080}$ in comparison with the other cases with winglet. So, it seems that the ratio 0.080 between length of winglet and the diameter of rear propeller is suitable for posture control.

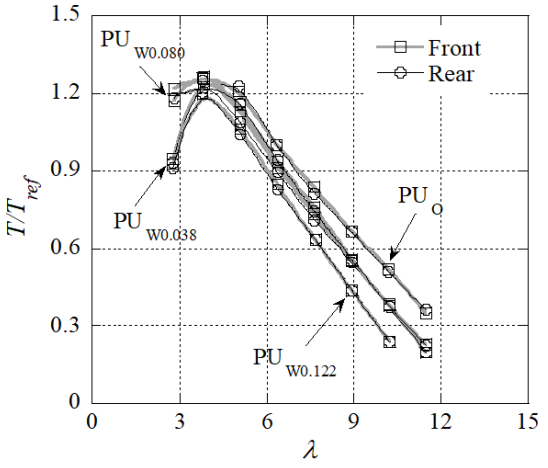

Fig. 4 Changes in torque ratio due to λ

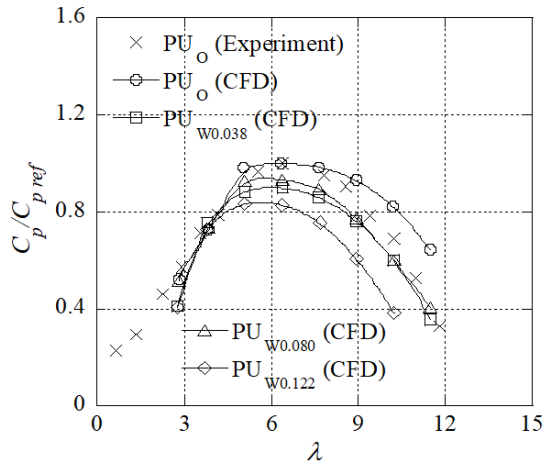

Fig. 5 Changes in power coefficient ratio

4. Conclusion

In this study, the effects of winglet length on posture and blade performance were investigated by circulation type water channel tests and CFD. As the result, it seems that the ratio 0.080 between length of winglet and the diameter of rear propeller is suitable for posture control.

A Study on Performance Improvement of Boil-off Gas Re-liquefaction Systems for LNG-fueled Ships

Jun-Seong Kim[1] ▪ Do-Yeop Kim [2] ▪ You-Taek Kim[†]

† Division of Marine System Engineering, Korea Maritime & Ocean University, 727 Taejong-ro, Yeongdo-Gu, Busan 49112, South Korea, kimyt@kmou.ac.kr

1 Division of Marine System Engineering, Korea Maritime & Ocean University, jskim87@kmou.ac.kr

2 Division of Marine System Engineering, Korea Maritime & Ocean University, doyeop@kmou.ac.kr

Key Words: LNG-fueled ship, Re-liquefaction system, Boil-off gas, LNG-fueled ship, N_2 reverse Brayton cycle, LNG cold energy

1. Introduction

Recently, regulations on environmental pollution from ships have been strengthened internationally [1]. LNG-fueled ships can reduce most pollutants, which is advantageous in responding to regulations [2]. Meanwhile, LNG-fueled ships require a boil-off gas (BOG) re-liquefaction system for condensing BOG generated from an LNG fuel tank [3]. In this study, research was conducted to improve the performance of the BOG re-liquefaction system for LNG-fueled ships.

2. System analysis

2.1 BOG Re-liquefaction system

Figure 1 is a BOG re-liquefaction system for LNG-fueled ships proposed by Kwak et al [3]. This system is characterized by applying the N_2 reverse Brayton cycle as a re-liquefaction method and using BOG compressors.

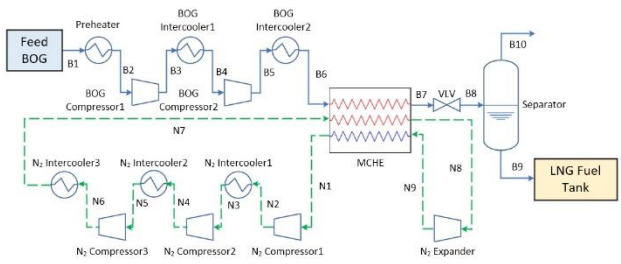

Figure 1. Schematic diagram of the BOG re-liquefaction system for LNG-fueled ship proposed by Kwak et al. [3]

Figure 2 is a system that applies LNG cold energy to the BOG re-liquefaction system based on the N_2 reverse Brayton cycle [4]. This system can be expected to improve thermodynamic performance through LNG cold energy.

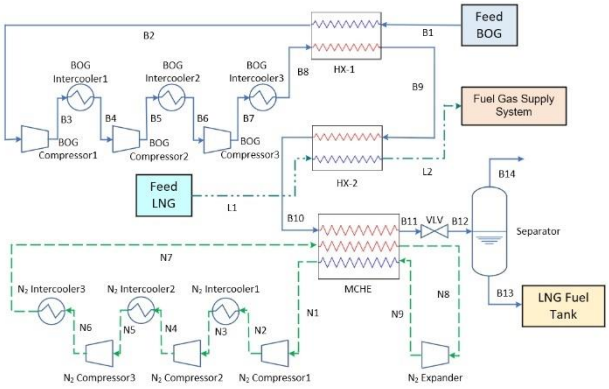

Figure 2. Schematic diagram of the BOG re-liquefaction system for LNG-fueled ship proposed using LNG cold energy [4]

In this study, each system was simulated using Aspen HYSYS v12.1 [5], and the thermodynamic performance was compared and analyzed.

2.2 Energy and exergy analysis

The thermodynamic performance of the BOG re-liquefaction system for LNG-fueled ships using LNG cold energy (Figure 2) was compared and analyzed with the Kwak's system (Figure 1). As performance indicators of the system, specific energy consumption (SEC) was used for energy analysis as shown in

Equation 1. In addition, for exergy analysis, exergy efficiency (η_{ex}) expressed as Equation 2 was examined [6].

$$SEC = \frac{\sum \dot{W}_c}{\dot{m}_{LBOG}} \quad (1)$$

$$\eta_{ex} = \frac{\dot{E}_{LBOG} - \dot{E}_{BOG}}{\sum \dot{W}_c} \quad (2)$$

2.3 BOG conditions

The conditions of BOG in the simulated system are referred to Ref. [3], and can be summarized as shown in Table 1.

Table 1. BOG conditions of the BOG re-liquefaction system for LNG-fueled ship

Variables	Unit	Value
Inlet mass flow	kg/h	83.3
Inlet pressure	kPa	160.0
Outlet temperature	°C	Saturated liquid condition
Outlet pressure	kPa	150.0

3. Results of system analysis

3.1 Energy analysis

Table 2 shows the energy analysis results for the system using LNG cold energy (Figure 2) and Kwak's system (Figure 1), respectively. The SEC of the system using LNG cold energy was 0.3 kWh/kg_{LBOG}, which was better than Kwak's system.

Table 2. Results of the energy analysis of BOG re-liquefaction system for LNG-fueled ship

System	Figure 1	Figure 2
SEC [kWh/kg_{LBOG}]	1.4	0.3

3.2 Exergy analysis

Table 3 shows the exergy analysis results for the system using LNG cold energy (Figure 2) and Kwak's system (Figure 1), respectively. The exergy efficiency (η_{ex}) of the system using LNG cold energy was 88.8 %, which was better than Kwak's system.

Table 2. Results of the exergy analysis of BOG re-liquefaction system for LNG-fueled ship

System	Figure 1	Figure 2
η_{ex} [%]	19.6	88.8

4. Conclusion

In this study, the performance improvement of the BOG re-liquefaction system for LNG-fueled ships was studied. A system that applied LNG cold energy to a BOG re-liquefaction system based on N_2 reverse Brayton cycle was shown.

The thermodynamic performance of this system was compared and analyzed with the re-liquefaction system proposed in Ref. [3]. As a result, the BOG re-liquefaction system using LNG cold energy showed a very significant performance improvement in energy and exergy analysis.

References

[1] Vedachalam, S., Baquerizo, N., and Dalai, A. K., 2022, "Review on impacts of low sulfur regulations on marine fuels and compliance options," Fuel, Vol. 310, pp. 122243.

[2] Son, H., and Kim, J.-K., 2019, "Operability study on small-scale BOG (boil-off gas) re-liquefaction processes," Energy, Vol. 185, pp. 1263–1281.

[3] Kwak, D.-H., Heo, J.-H., Park, S.-H., Seo, S.-J., and Kim, J.-K., 2018, "Energy-efficient design and optimization of boil-off gas (BOG) re-liquefaction process for liquefied natural gas (LNG)-fuelled ship," Energy, Vol. 148, pp. 915–929.

[4] Kim, J.-S., and Kim, D.-Y., 2023, "Energy, Exergy, and Economic (3E) Analysis of Boil-Off Gas Re-Liquefaction Systems Using LNG Cold Energy for LNG-Fueled Ships," J. Mar. Sci. Eng., Vol. 11, pp. 587.

[5] AspenTech, 2021, HYSYS User's Guide, Release V12.1, Bedford, MA, USA.

[6] Shen, J., Yan, S., Li, Z., Xiao, Y., and Tan, N., 2021, "Design and analysis of boil-off gas reliquefaction processes for the LNG-fueled ships," Applied Thermal Engineering, Vol. 199, pp. 117505.

Flame Surfaces Variation through Ionic Wind and Flame Stretch in Mass-Diffusively Unstable Flame

Siyeong Yu[1, 2)], Dae Geun Park[3)], Sung Hwan Yoon[1, 2)]

Department of Marine System Engineering, Korea Maritime and Ocean University, 727 Taejong-ro, Yeongdo-gu, Busan, 49112, Republic of Korea[1)]
Interdisciplinary Major of Maritime AI Convergence, Korea Maritime and Ocean University, 727 Taejong-ro, Yeongdo-gu, Busan, 49112, Republic of Korea[2)]
Carbon Neutral Technology R&D Department, Korea Institute of Industrial Technology (KITECH), 89 Yangdaegiro -gil, Seobuk-gu, Cheonan, 31056, Republic of Korea[3)]

Electrically assisted combustion is a novel approach to combustion technology that utilizes electricity, contributing to the reduction of soot, increase of flame propagation speed, control of flame surface area, and flame stabilization[1)]. In particular, the reduction of soot can improve incomplete combustion, aligning with the main interest of the maritime industry, which is actively focused on emission reduction. Additionally, while existing combustion systems regulated output by supplying more fuel to achieve higher power, our team aims to propose a newly proposed combustion system using electrically assisted combustion.

One of the most representative phenomena in electrically assisted combustion is ionic wind. When a flame is putted in the electric field, charges by chemi-ionization are accelerated to corresponding electrode by the Lorentz force. Then, charges diffuse a collisional momentum to neutrons, which account for 90% of production by chemi-ionization, during their acceleration. Consequently, neutrons are move to electrodes with charges, and it is called ionic wind[2)].

Using a combustor made from an acrylic tube, our research team applied electric fields to downward-propagating premixed flames in stationary mixture, resulting in significant changes in flame displacement velocity and flame surface area. Also, detailed information regarding flame area variations with different types of fuels, dilution gases, and applied voltages will be presented through an oral presentation.

References

(1) Park, D.G., Chung, S.H., Cha, M.S., “Dynamic responses of counterflow nonpremixed flames to AC electric field.” Combust. Flame, 198, pp.240-248, 2018.
(2) Park, D.G., Chung, S.H., Cha, M.S., “Visualization of ionic wind in laminar jet flames.” Combust. Flame, 18, pp. 246-248, 2017.

Research on buoy shape to improve wave energy conversion efficiency

Takuma IMAIZUMI[*1], Yasutaka IMAI[*2] and Shuichi NAGATA[*3]

[*1]Department of Science and Engineering, Saga University

[*2,*3] Institute of Ocean Energy, Saga University

1. Introduction

We are currently conducting research on the practical application of a floating oscillating water column wave power generation device called a "back bending duct buoy". This device, proposed by Masuda, consists of a buoyant body, an L-shaped duct, an air chamber, and a turbine/generator, as shown in Figure 1. Wave energy is converted into air energy that moves in and out of the air chamber to the turbine through the oscillating water column in the duct of the BBDB, which is agitated by the waves (primary conversion), and then converted into electrical energy by the turbine/generator (secondary conversion). In order to design floating OWC (Oscillating Water Column)-type wave energy converter such as Backward Bent Duct Buoy (BBDB), it is necessary to develop a numerical method to make clear an optimal hull shape which maximizes the generating electrical energy. Therefore, this study proposes a two-dimensional analysis method that can evaluate the first-order conversion performance of floating oscillating water-column wave power generators such as BBDBs in regular waves. In this study, the boundary element method based on velocity potentials is used for the analysis of water, while the equation of state, mass conservation law, and energy conservation law are used for the analysis of air in the air chamber. From these equations, motions of floating body, air pressure in air chamber, transmission and reflection coefficient of water waves and primary conversion efficiency are calculated.

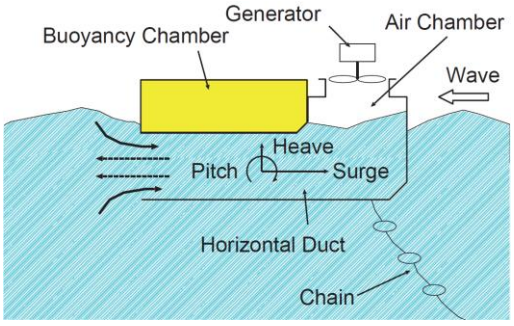

Fig.1 BBDB overview

2. Analysis Model

The analytical model considered in this study is shown in Figure 2. The water depth is assumed to vary arbitrarily from h~h', the floating body is moored by n* linear springs, and a nozzle of diameter D is assumed to be installed in the ceiling of the air chamber. The origin is on the surface of the still water, the x-axis is horizontal and the z-axis is vertical, and the coordinates of the center of gravity of the floating body at rest are $G(\overline{x_0}, \overline{z_0})$ and $Q(x_b, z_b)$. Assume that the center of gravity of the floating body at time t is at (x_0, z_0), and that it receives incident waves of angular frequency σ and amplitude ζ_0, and translates in the x- and z-directions by ξ and η, respectively, and rotates clockwise by an angle θ. If the complex amplitudes of the horizontal displacement, vertical displacement, and rotation angle are X, Y, and Θ, respectively, the motion of the floating body can be expressed as follows,

$$\zeta = x_0 - \overline{x_0} = Re\left[X \cdot e^{i\sigma t}\right]$$
$$\eta = z_0 - \overline{z_0} = Re\left[Z \cdot e^{i\sigma t}\right]$$
$$\theta = Re\left[\Theta \cdot e^{i\sigma t}\right]$$

where $i = \sqrt{-1}$ and Re denotes the real part.

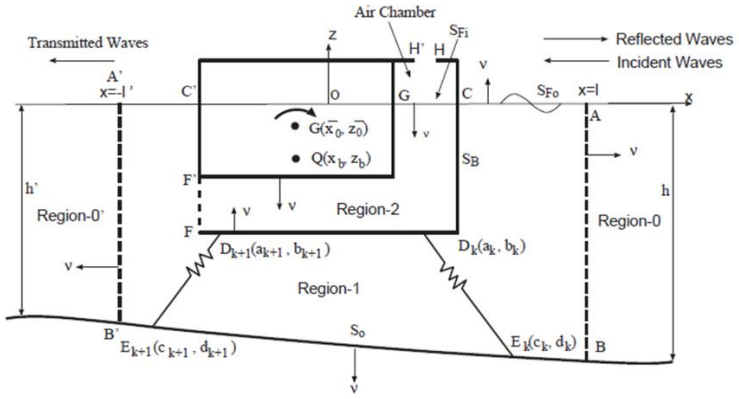

Fig3 Analysis model

If we delimit the fluid domain by setting virtual boundaries AB, A'B', and FF' as shown in Figure 2, the velocity potentials of each domain can be expressed as follows.

・Region-1

$\nabla^2\phi^{(1)} = 0$ (Inside Fluid)

$\frac{\partial\phi^{(1)}}{\partial v} = \frac{\sigma^2 h}{g}\phi^{(1)}$ (Free surface: external)

$\frac{\partial\phi^{(1)}}{\partial v} = 0$ (Bottom)

$\frac{\partial\phi^{(1)}}{\partial v} = \frac{\sigma^2 h}{g}\left[\frac{X}{\zeta_0}\frac{dz}{ds} - \frac{Z}{\zeta_0}\frac{dx}{ds} - \frac{\Theta h}{\zeta_0}\left\{(x-\overline{x_0})\frac{dx}{ds} + (z-\overline{z_0})\frac{dz}{ds}\right\}\right]$ (On Body surface)

$$\begin{cases} \phi^{(1)}(l,z) = \left[e^{i\lambda l} + K_r e^{-i\lambda l}\right]A(\lambda z) \\ \frac{\partial\phi^{(1)}}{\partial v}(l,z) = i\lambda\left[e^{i\lambda l} - K_r e^{-i\lambda l}\right]A(\lambda z) \end{cases} \quad A(\lambda z) = \frac{\cosh\lambda(z+1)}{\cosh\lambda}$$ (Incident wave + Reflected wave)

$$\begin{cases} \phi^{(1)}(-l',z) = K_t e^{-i\lambda l'}A(\lambda' z) \\ \frac{\partial\phi^{(1)}}{\partial v}(-l',z) = -i\lambda K_t e^{-i\lambda l'}(\lambda' z) \end{cases} \quad A(\lambda' z) = \frac{\cosh\lambda'(z+h')}{\cosh\lambda\, h'}$$ $(Transmission\ wave)$

where K_r and K_t are complex constants for reflectance and transmittance, respectively.

・Region -2

$\nabla^2\phi^{(2)} = 0$ (Inside Fluid)

$\frac{\partial\phi^{(2)}}{\partial v} = \frac{\sigma^2 h}{g}\left\{ip_s^a - \left(1 - i\frac{\mu}{\sigma}\right)\phi^{(2)}\right\}$ (On the free surface: internal)

$\frac{\partial\phi^{(1)}}{\partial v} = \frac{\sigma^2 h}{g}\left[\frac{X}{\zeta_0}\frac{dz}{ds} - \frac{Z}{\zeta_0}\frac{dx}{ds} - \frac{\Theta h}{\zeta_0}\left\{(x-\overline{x_0})\frac{dx}{ds} + (z-\overline{z_0})\frac{dz}{ds}\right\}\right]$ (On the floating surface)

・**Connection condition between Region-1 and Region-2**

$\phi^{(1)} = \phi^{(2)}, \frac{\partial \phi^{(1)}}{\partial \upsilon} = \frac{\partial \phi^{(2)}}{\partial \upsilon}$

3. Calculation

The calculations are performed by coupling the boundary integral equations for the fluid section, the equations for the air in the air chamber, and the equations of motion for the floating body.

・**Boundary integral equations**

The boundary line surrounding the fluid is decomposed into N micro line segments, the center coordinates of each element are denoted by (ξ_j, η_j) $(j = 1 \sim N)$, and the length of the line segment is Δs_j.

Assuming that the potential function and its normal derivative at each element are constant, the following relationship between the potential function value $\phi(j)$ and its normal derivative $\bar{\phi}(j)$ at each point is established from Green's formula.

$$\sum_{j=1}^{N}\left[F_{mj} \cdot \phi(j) - E_{mj} \cdot \bar{\phi}(j)\right] = 0 \qquad (\mathrm{m} = 1 \sim \mathrm{N}) \qquad (1)$$

where,

$F_{mj} = -\delta_{mj} + \bar{E}_{mj} \quad (\mathrm{Region} - 1), \quad F_{mj} = \delta_{mj} + \bar{E}_{mj} \quad (\mathrm{Region} - 2)$

$E_{mj} = \frac{1}{\pi}\int_{\Delta S_j} \log R_{mj} ds$, $\bar{E}_{mj} = \frac{1}{\pi}\int_{\Delta S_j} \frac{\partial}{\partial \nu} \log R_{mj} ds$, $R_{mj} = \left[\left(\xi_j - \xi_m\right)^2 + \left(\eta_j - \eta_m\right)^2\right]^{1/2}$

δ_{mj} is the Kronecker delta.

Substituting the boundary condition equations obtained in Chapter 2 into Equation 2, we obtain the algebraic equations for Regions -1 and 2.

・**Equations for the air in the air chamber**

From the equation of state, the law of conservation of mass, and the law of conservation of energy, establish the basic equation for the motion of air in an air chamber.

The equation of state： $p_a = \rho_a R T_a$ (2)

The law of conservation of mass： $\frac{d}{dt}\left(\frac{p_a V_a}{R T_a}\right) + \frac{dm_a}{dt} = 0$ (3)

The law of conservation of energy： $\boldsymbol{p_a} \frac{dV_a}{dt} + C_v \frac{d}{dt}\left(\frac{p_a V_a}{R}\right) + C_p T_e \frac{dm_a}{dt} = 0$ (4)

where,

$\frac{dm_a}{dt} = \pm \rho_e \varepsilon C_d C_s A_W \sqrt{2C_p |T_a - T_0|}$

p_a：Air chamber pressure, T_a：Chamber temp, V_a：Chamber Volume, t：time, dm_a/dt：Mass outflow rate of air, R：Gas constant, C_v：specific heat of formation, C_p：specific heat at constant pressure, ε：Nozzle ratio, C_d：contraction coefficient, C_s：velocity coefficient

Linearizing and rearranging Equations 2~4 yields the basic Equation 5.

$$\sum_{j=1}^{N_1^{(2)}}\left(1 - i\frac{\mu}{\rho}\right)\phi_1^{(2)}(j) \cdot \Delta x_j - \frac{(1 + iC_E) l_C}{C_E} p_s^a - i l_C (x_{0r} - \overline{x_0}) \frac{\Theta h}{\zeta_0} = 0 \qquad (5)$$

・**The equations of motion for the floating body**

The equation of motion of a floating body is formulated separately for surge, heave, and pitch.

$M\frac{d^2(Xe^{i\sigma t})}{dt^2} = P_X^{(w)} + F_X + P_X^{(a)}, M\frac{d^2(Ze^{i\sigma t})}{dt^2} = P_Z^{(w)} + P_Z^{(s)} + F_Z + P_X^{(a)}, M\frac{d^2(Ze^{i\sigma t})}{dt^2} = P_Z^{(w)} + P_Z^{(s)} + F_Z + P_X^{(a)}$

where,

$P_X^{(w)}, P_Z^{(w)}, T_\theta^{(w)}$: Fluid power by water, $P_Z^{(s)}, T_\theta^{(s)}$: Static Righting Moment,

F_X, F_Z, M_θ : Mooring force, $P_X^{(a)}, P_Z^{(a)}, T_\theta^{(a)}$: Air pressure acting on air chamber wall

Equation 6 is obtained from the boundary integral equation and the equation of motion of the BBDB.

$\phi_1^{(2)}(j) = C_j^{(1)} P_S^{(a)} + d_j^{(1)}$ (6)

$K_t = C^{(2)} P_S^{(a)} + d_j^{(2)}$

$X/\zeta_0 = C^{(3)} P_S^{(a)} + d_j^{(3)}$ $etc.$

Substituting Equation 6 into Equation 5 yields Equation 7 for the air chamber pressure amplitude.

$$C_1 P_S^{(a)} + B_2 \frac{P_S^{(a)}}{\sqrt{\left|P_S^{(a)}\right|}} + C_3 = 0 \quad (7)$$

Since C_1, B_2, and C_3 are constants in the above equation, $P_S^{(a)}$ is obtained by iterative calculation. Equation 6 and other equations are then used to obtain the potential on the fluid boundary and its normal direction derivative, the wave transmission coefficient, and the motion of the floating body.

4. Conclusion

Using these methods, we obtained the primary conversion efficiency and motion of the BBDB.

Correlation between Ionic Wind and Thermo-Acoustic Instability in Downward-Propagating Premixed Flame under Electric

Dae won Im[1)], Dae Geun Park[3)], Sung Hwan Yoon[1, 2)]

Department of Marine System Engineering, Korea Maritime and Ocean University, 727 Taejong-ro, Yeongdo-gu, Busan, 49112, Republic of Korea[1)]
Interdisciplinary Major of Maritime AI Convergence, Korea Maritime and Ocean University, 727 Taejong-ro, Yeongdo-gu, Busan, 49112, Republic of Korea[2)]
Carbon Neutral Technology R&D Department, Korea Institute of Industrial Technology (KITECH), 89 Yangdaegiro -gil, Seobuk-gu, Cheonan, 31056, Republic of Korea[3)]

The recent incidents involving the explosion of spacecraft developed by NASA and SpaceX have once again sparked global interest in the stability of rocket engines. Among the significant challenges in rocket engine development, thermoacoustic instability stands out, rooted in the fundamental coupling of rapid heat release from combustion and inherent resonances within the combustion chamber[1)]. This phenomenon, which can lead to compromised engine lifespan and, in extreme cases, catastrophic failure, necessitates the analysis of the combustion chamber's inherent natural frequencies to induce a phase mismatch between thermal energy and pressure waves, thus ensuring combustion system stability[2)].

To address these challenges, various studies have been undertaken to mitigate combustion instability within the combustion chamber, encompassing the development of injector array patterns, combustion stabilization mechanisms such as baffles, acoustic cavities, and Helmholtz resonators[3, 4)].

This research team aims to propose a novel ap proach utilizing electric fields to mitigate combus tion instability. Employing electric fields enables active control, effectively suppressing thermoacous tic instability. Furthermore, it facilitates simplifica tion of internal engine components. Detailed expe rimental conditions and results are intended to be presented through the publication.

References

(1) J. Rayleigh, “The explanation of certain acoustical phenomena.” Nature, 18 ,1878, pp. 319-321.
(2) C. Lieuwen, V. Yang, “Combustion instabilities in gas turbine engines.” AIAA, 2005.
(3) D.T Harrje, F.H. Reardon, “Liquid Propellant Rocket Combustion Instability.” NASA Special Publication, 1972. pp.194.
(4) D. Zhao and A.S. Morgans, “Tuned passive control of combustion instability using multiple Helmholtz resonators.” J. Sound and Vibration, 320, 2009, pp.744-757.

Study of Power Generation System Utilizing Waste Heat from Marine Engine (Possibility of introducing HFO Refrigerant)

Atsuyoshi ETSUKAWA*1, Junichi OHARA*1, Hideyuki YOSHIMURA*1, Masaki ARIYOSHI *1, Yoshihiro SHIMAOKA*2 and Yasuyuki IKEGAMI*3

National Fisheries University, 2-7-1 Nagatahonmachi, Shimonoseki-shi, Yamaguchi 759-6595, Japan*1
National Institute of Technology, Toba College1-1 Ikegami, Toba-shi, Mie 517-8501, Japan*2
Institute of Ocean Thermal Energy, Saga University, 1-Honjomachi, Saga−shi, Saga 840-8502, Japan*3

Abstract

In the present study, the characteristics of cycle thermal efficiency and net power output were clarified for a marine waste heat power generation system to verify if HFO refrigerant (HFO-1234yf, HFO-1233zd(E)), which is a green refrigerant, can be a substitute for HFC refrigerant when HFC refrigerant (HFC-134a, HFC-245fa), which will no longer be used, is employed. When the heat source temperature, flow rate, and heat transfer performance of the heat exchanger are defined, HFO-1233zd(E) and HFO-1234yf show almost the same turbine output values obtained compared to conventionally used HFC-245fa and HFC-134a. Therefore, HFO-1233zd(E) should be adopted in this power generation system as an alternative refrigerant to HFC-245fa and HFC-134a, which are conventionally used.

Key Words: Waste Heat Energy, Marine Engine, Turbine Output, Rankine Cycle, Green Working Fluid

1. Introduction

Recent years in particular, the regulation of greenhouse gas emissions for the control of global warming is being tightened for the operation of ships[1]. As one of the countermeasures, Exhaust heat temperature difference power generation, which recovers and effectively utilises the exhaust heat from marine engines, is attracting attention. There are few research results on power generation systems using unregulated green refrigerants. Therefore, this study clarifies the characteristics of cycle thermal efficiency and net power output for marine waste heat power generation systems to verify whether HFO refrigerant can be a substitute for HFC refrigerant when HFC refrigerant (HFC-134a, HFC-245fa) and green refrigerant (HFO-1234yf, HFO-1233zd(E)), which will no longer be available, are employed.

2. Binary power generation system of Rankine Cycle using waste heat from marine engine

Figure 1 shows the outline of a binary power generation system of organic rankine cycle, utilizing waste heat from marine engine. Binary power generation generally utilizes steam or hot water at 80 to 150°C as a heat source (primary system) to heat and evaporate a low-boiling working fluid (secondary system) and utilize the steam to turn the turbine to generate electricity. Hot water from marine engine is utilized as the high heat source and seawater is utilized as the low heat source. The numbers 1 to 4 in the diagram indicate the state points between each component.

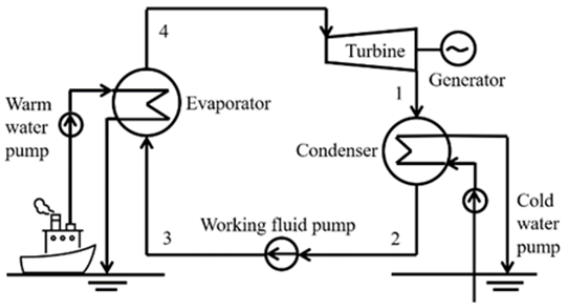

Fig. 1 Power Generation System Utilizing Waste Heat from Marine Engine

Table 1 Thermophysical properties of working fluids

Working fluid	Chemical formula	Boiling point [℃]	Heat of vaporization [kJ/kg]	ODP	GWP
HFO-1234yf	$C_3H_2F_4$	−29.0	145.2	0	<1
HFO-1233zd (E)	$C_3H_2F_3Cl$	19.0	194.0	0	<1
HFC-134a	CH_2FCF_3	−26.1	217.0	0	1,430
HFC-245fa	$C_3H_3F_5$	15.3	190.9	0	950

Table 2 Calculated conditions

Input Data		
Warm water inlet temperature	T_{WWI}	90.0 [℃]
Warm water outlet temperature	T_{WWO}	40.0～80.0 [℃]
Cold water inlet temperature	T_{CWI}	20.0 [℃]
Cold water outlet temperature	T_{CWO}	30.0 [℃]
Flow rate of warm water	m_{WW}	20 [kg/s]
Flow rate of cold water	m_{CW}	Calculated through convergence
Heat conductance of evaporator	$(UA)_E$	200,400 [kW/K]
Heat conductance of condenser	$(UA)_C$	200,400 [kW/K]

3. Relational expression used in cycle calculations

The equations used in the cycle calculations in this report are given below. The cycle thermal efficiency and turbine power are defined by the following equations.

$$\eta_{th} = \frac{W_T - W_P}{Q_E} = \frac{(h_4 - h_1) - (h_3 - h_2)}{h_4 - h_3} \quad (1)$$

$$W_T = m_{WF}(h_4 - h_1) \quad (2)$$

W_T indicates turbine output, W_P indicates pump output and Q_E indicates evaporator exchange heat rate. h_1, h_2, h_3 and h_4 are the specific enthalpies at the turbine outlet, condenser outlet, evaporator inlet and turbine inlet in Figure 1, respectively, and m_{WF} is the refrigerant flow rate.

4. Calculation Conditions and Methods

Table 1 shows the refrigerants evaluated and the thermodynamic properties of each working fluid compared. REFPROP[2)] was used to calculate these physical properties. The calculation conditions for the cycle calculations in this study are shown in Table 2. The cold water flow rate is obtained by convergence calculations in the heat balance on the condenser side. The cycle thermal efficiency and turbine power are calculated by changing the heat transfer performance of the evaporator and condenser to 200 W/K and 400 W/K, respective.

5. Calculation Results and Considerations

5・1 Evaluation of Thermophysical Properties

Figure 2 shows the *P-h* diagram for each refrigerant. Figure 2 shows that HFO-1233zd(E) and HFC-245fa have similar thermophysical properties. In addition, HFO-1234yf and HFC-134a have similar thermophysical properties, although there is a difference in latent heat content. Focusing on adopting a refrigerant in this power generation system, HFO-1233zd(E) and HFC-245fa, which have low pressure and high latent heat, should be used.

Figure 3 shows the *T-s* diagram for each refrigerant. Figure 3 shows that HFO-1233zd(E) and HFC-245fa have similar thermophysical properties, as in Figure 2. In addition, HFO-1234yf and HFC-134a have similar thermophysical properties, although there is a difference in entropy. Focusing on adopting a refrigerant in this power generation system, HFO-1233zd(E) and HFC-245fa, which have large entropy difference, should be used.

5・2 Assessment of turbine power versus refrigerant flow rate

Figure 4 shows that the turbine power value changes convexly upward as the refrigerant flow rate changes, and that the turbine power values obtained with HFO-1233zd(E) and HFO-1234yf are almost equivalent to those obtained with HFC-245fa and HFC-134a, which are conventionally used. There is an optimum value of refrigerant flow rate at which the turbine output value is the highest, and it is smaller for HFO-1233zd(E), HFC-245fa, HFC-134a, and HFO-1234yf, in that order.

The above results indicate that the lower the refrigerant flow rate, the lower the refrigerant circulation pump power, which may affect the net power output of the entire system, depending on the scale of the power generation system. Therefore, HFO-1233zd(E) and HFO-1234yf can be adopted as alternative refrigerants to HFC refrigerants.

6. Conclusions

1) When the heat source temperature, flow rate, and heat transfer performance of the heat exchanger are defined, HFO-1233zd(E) and HFO-1234yf show almost the same turbine output values obtained compared to conventionally used HFC-245fa and HFC-134a.
2) Similar to HFC-245fa, HFO-1233zd(E) has operating conditions where the turbine output peaks at a lower refrigerant flow rate than HFO-1234yf or HFC-134a. The lower refrigerant flow rate results in lower refrigerant circulation pump power, which may affect the net power output obtained by the entire system, depending on the scale of the power generation system.
3) The ratio of refrigerant circulation pump power to turbine power was small for each refrigerant, and had no effect on net power output. Therefore, HFO-1233zd(E) and HFO-1234yf have the potential to be adopted as alternative refrigerants to HFC refrigerants.

References

1) Yasunobu Araki, "Energy Efficiency Design Index (EEDI) Regulations and Corresponding Technology Trends", Journal of the Japan Institute of Marine Engineering. Vol. 52, No. 4 (2017), pp. 480-484.
2) NIST：REFPROP Version 10.0，(2018).

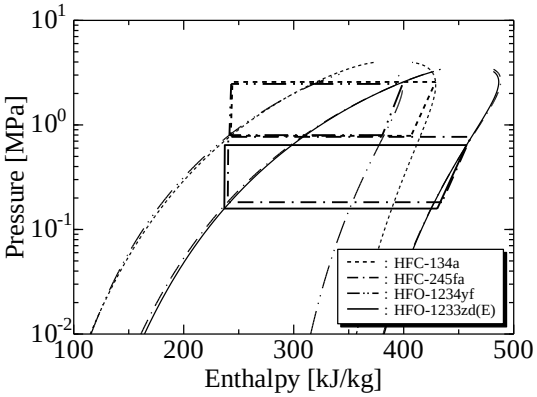

Fig. 2 *P* - *h* diagram

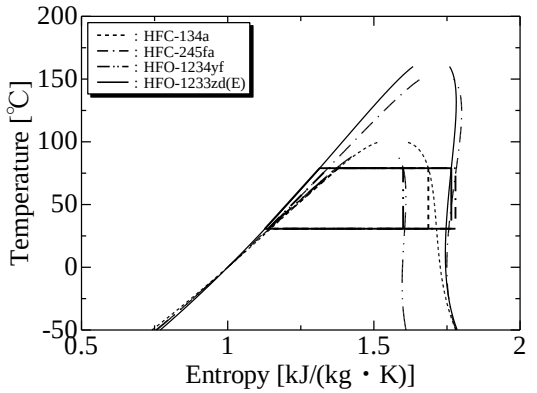

Fig. 3 *T* - *s* diagram

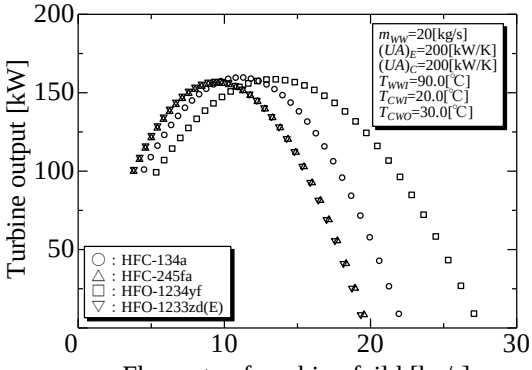

Fig. 4 Characteristics of Turbine output for variable Flow rate of working fluid

Combustion field measurement of temperature, concentration and velocity using TDLAS

Jeong Woong Hong[1, 2)], Min Gyu Jeon [3)] Sung Hwan Yoon[1, 2)]

Department of Marine System Engineering, Korea Maritime and Ocean University, 727 Taejong-ro, Yeongdo-gu, Busan, 49112, Republic of Korea[1)]
Interdisciplinary Major of Maritime AI Convergence, Korea Maritime and Ocean University, 727 Taejong-ro, Yeongdo-gu, Busan, 49112, Republic of Korea[2)]
Department of Mechanical Engineering, Republic of Korea Naval Academy, Changwon 51704, Republic of Korea[3]

Tracking and monitoring greenhouse gases emitted from industries to comply with environmental regulations is becoming increasingly important. In response, research and development of power units that increase combustion efficiency, and the use of low-carbon fuels such as LNG, hydrogen, and ammonia are being conducted. To accurately diagnose the combustion state and combustion efficiency, it is necessary to track the combustion products generated by the combustion reaction. Temperature, concentration, and speed are important factors to check the combustion efficiency of the flame.

However, current measurement methods have limitations. Such as, temperature measurement using thermocouple and velocity measurement using hot-wire anemometer are contact to measuring area, it is cuased error by thermal radiation. And non-contact optical techniques such as CARS(Coherent anti-Stokes Raman Spectroscopy) and LIF(Laser Induced Fluorescence) are expensive and complex optical systems.

In this study, we aimed to confirm the possibility of non-contact measurement technology in places where direct measurement is impossible. We used TDLAS (Tunable Diode Laser Absorption Spectroscopy) [(1-3)], a wavelength-variable absorption spectroscopy system, to measure temperature, concentration, and velocity simultaneously in combustion field. And we arranged various types of cells for gas supply flow conditions, temperature, concentration, and velocity measurements, and compared the measurement results to confirm the possibility of simultaneous measurement. Details on the experimental method and results will be intend to through the presentation.

References

(1) Y. Zaatar, J. Bechara, A. Khoury, D. Zaouk and J. P. Charles, Diode laser sensor for process control and environmental mon-itoring, Applied Energy, 65 (1) (2000) 107-113
(2) M.G. Jeon, J. W. Hong, K. M. Kim and D. H. Doh, Development of measurement technique of explosive flame using an optical measurement method, Journal of Mechanical Science and Technology 34(21) (2020) 5109-5115
(3) M. G. Jeon, D. H. Doh and Y. deguchi, Optical temperature measurement method of premixed flames using a multi-laser system, Journal of Mechanical Science and Technology 35(6) (2021) 2535-2542

Tip clearance gap effect on the hydraulic performance of a mixed flow pump with semi-open casing

Ujjwal Shrestha
Department of Mechanical Engineering, Mokpo National University
Muan, 58554, Republic of Korea, ujjwalshrestha10@yahoo.com

Young-Do Choi
Department of Mechanical Engineering, Institute of New and Renewable Energy, Mokpo National University
Muan, 58554, Republic of Korea, ydchoi@mnu.ac.kr

Abstract

Mixed-flow pumps are widely used in agriculture, water conservancy, shipping, power, and other industries due to the advantages of high flow rate, high efficiency, and cavitation resistance. The tip clearance gap between the blade tip and shroud is inevitable in fluid machinery. The tip clearance gap can induce leakage flow and interact with the mainstream flow, which causes efficiency drop and cavitation in hydraulic machinery. The pressure fluctuation is associated with the stable operation of hydraulic machinery, and leakage flow induces the unstable flow pattern and increases the pressure fluctuation amplitude in the hydraulic machinery. The concept of clearance gap is unique in a mixed flow pump with a semi-open casing. The systematic investigation of the hydraulic and suction performance of a mixed flow pump with a semi-open casing is rarely performed. In the present work, a detailed analysis is conducted to evaluate the influence of the tip clearance gap on the performance curves, pressure fluctuations, and vortex intensity. Figure 1 shows the performance curves of a mixed-flow pump with various clearance gaps. Figure 2 shows the leakage flow in the mixed-flow pump. The reverse flow from the high-pressure region to the low-pressure zone is observed in the clearance gap. The magnitude of reverse flow increases with an increase in clearance gap width. The clearance gap shows a significant influence on the hydraulic and suction performance in the mixed flow pump with a semi-open casing. The leakage flow is dependent on the width of the clearance gap between the blade tip and the shroud wall. The efficiency and head of the mixed flow pump decreased significantly with an increase in the clearance gap.

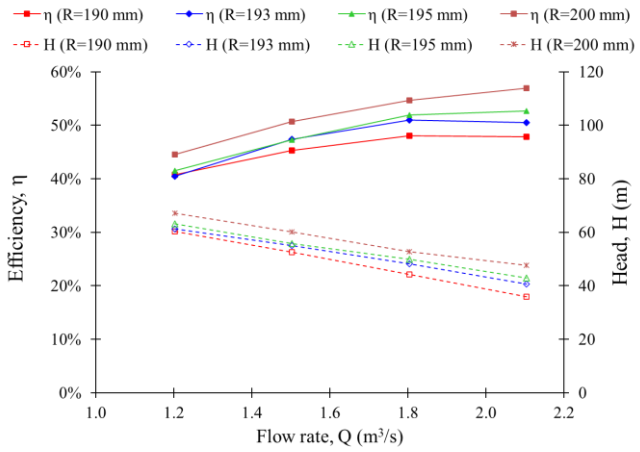

Figure 1 Effect of clearance gap on semi-open mixed flow pump performance curves

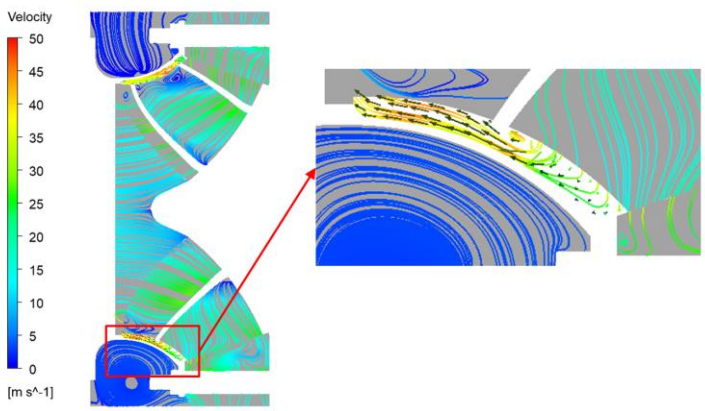

Figure 2 Velocity vectors on the leakage gap

A study of fuel cell-battery propulsion system for four types of vessels

Jong In Kim[1] · San Kim[2] · Eun Shin Bang[3] · Kyoung Kuk Yoon[4] · Sang Kyun Park[†]

The shipping industry accounts for a large proportion of global carbon emissions, and various methods are being tried to reduce these emissions. One of the methods is to replace the existing internal combustion engine, which is the power source of the ship, with a fuel cell. Among many fuel cells, Polymer Electrolyte Membrane Fuel Cell (PEMFC) produces power using a chemical reaction between hydrogen and oxygen, does not cause environmental pollution, and is used for small cars and public transportation on land because of its high efficiency and difficult operating conditions. Considering this usability, it would not be a long way to apply PEMFC to ships.

In theory, PEMFC has a high efficiency of about 60%, and it is easy to maintain/manage at an operating temperature of 70 to 80℃. In addition, it has the advantage of being able to respond quickly to the rapidly changing operating load of the ship due to its high reactivity. There have been cases in which small cruise ships with PEMFC have been operated overseas, but in Korea, ships using fuel cells as power sources have not yet been operated. In order for ships powered by fuel cells to be generalized and built in the future, related research needs to be sufficiently preceded.

In this study, four types of ships were identified, with PEMFC as the main power source and Li-ion batteries as auxiliary power sources for mutual supplementation in order to establish a ship system to which fuel cells are applied. The required output size and hull size were calculated according to the size and characteristics of each ship, the sizes of PEMFC and Li-ion batteries were designated accordingly, and a power system including a Balance of plant (BOP) was proposed. Fuel cells and batteries mainly play the role of base load and peak shaving, and propulsion motors and BOPs were configured depending on the size of the ship's power. The fuel cell was modularized with 50kW PEMFC and arranged according to the size of the ship, and redundancy of the power system was applied.

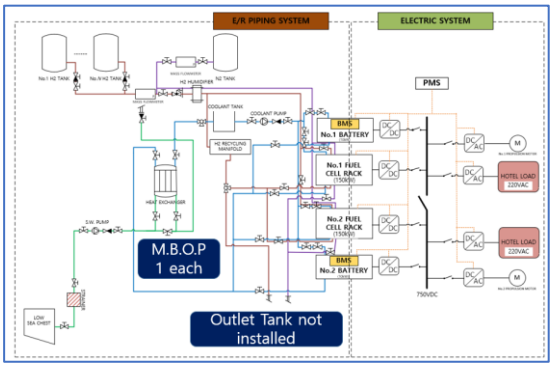

Fig.1 Piping and electric diagram of Leisure vessel

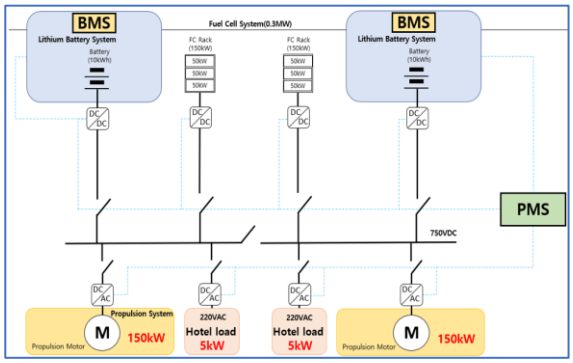

Fig.2 Electric propulsion system of Leisure vessel

† Corresponding Author: Professor, Division of Maritime AI & Cyber Security, Korea Maritime & Ocean University, E-mail: skpark@kmou.ac.kr
1 Researcher, Division of Marine Information Technology, Korea Maritime & Ocean University, E-mail: darkkrow@kmou.ac.kr
2 Researcher, Division of Marine Information Technology, Korea Maritime & Ocean University, E-mail: ks9524@g.kmou.ac.kr
3 Researcher, Korea Maritime & Ocean University, E-mail: esbang627@ kmou.ac.kr
4 Professor, Division of Maritime AI & Cyber Security, Korea Maritime & Ocean University, E-mail: kkyoon@kmou.ac.kr

POSTER

PRESENTATION

Characteristics of HFO Refrigerants in Double-Stage Reverse Rankine Cycle Refrigerator

Tetsuya HONDA[1)], Takafumi KOJIMA[1)] Junichi OHARA[1)], Hideyuki YOSHIMURA[1)],
Masaki ARIYOSHI[1)], Takafumi MORISAKI[2)] and Yasuyuki IKEGAMI[2)]

National Fisheries University, 2-7-1 Nagatahonmachi, Shimonoseki-shi, Yamaguchi 759-6595, Japan [1)]
Institute of Ocean Thermal Energy, Saga University, 1-Honjomachi, Saga−shi, Saga 840-8502, Japan[2)]

Abstract

The Kigali Amendment to the Montreal Protocol (effective 2019) regulates HFC refrigerants and other CFC substitutes with high global warming potential, and there is a need to convert to green refrigerants with low global warming potential. Therefore, in this study, cycle simulations of a double-stage reverse Rankine cycle using HFO1233zd(E), HFO1234yf, and HFO1234ze(E), Ammonia, and HFC32 were conducted to evaluate refrigerant performance under certain heat source conditions. As a result, in descending order of COP, they were HFO1233zd(E), Ammonia, HFC32, HFO1234ze(E), and HFO1234yf, and HFO1233zd(E) could be operated most efficiently.

Key Words: Reverse Rankine Cycle, Refrigerator, Double-Stage, HFOs, COP

1. Introduction

The Kigali Amendment led to the international regulation of CFC substitutes with high global warming potential (GWP). Therefore, it is necessary to convert to refrigerants with low GWP and to research refrigeration and air-conditioning equipment using low GWP refrigerants[1)].

Energy-saving and high-efficiency systems for refrigeration cycles have been proposed, and this study focuses on the multi-stage reverse Rankine cycle. A multistage reverse Rankine cycle is configured with two or more reverse Rankine cycles working between one low-temperature and one high-temperature heat source. Saga University group researches on this multistage reverse Rankine cycle and clarify these performances better than other typical refrigeration cycles [2)].

The system characteristics and refrigerant properties of the new HFOs-as green refrigerants and natural refrigerants have not yet been fully clarified.

This study investigates the refrigerant performance of the double-Stage reverse Rankine cycle using cycle simulations applied under certain heat source conditions for refrigerants: HFO1233zd(E), HFO1234yf, and HFO1234ze(E), Ammonia, HFC32.

2. Double-Stage reverse Rankine cycle

Figure 1 shows a conceptual *T-s* diagram of a Double-stage Reverse Rankine cycle. To increase COP in a basic reverse Rankine system, it is important to keep compression power lower relative to heat absorption and dissipation. For the attainment of this purpose, it is necessary to increase the heat transfer performance of the heat exchanger and reduce the temperature difference between the heat source and the working fluid.

As shown in Figure 1, the temperature difference between the heat source and the working fluid during the heat exchange process is reduced by using a double-stage inverted Rankine cycle, which is expected to improve the system performance.

Figure 2 shows a system schematic of the double-stage Reverse Rankine cycle. Two reverse Rankine cycles are installed in series for the high and low temperature heat sources, each cycle has its own evaporator, condenser, compressor.

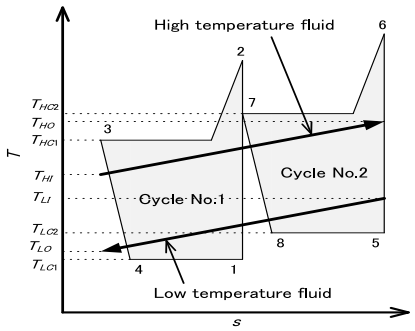

Fig.1 T-s diagram

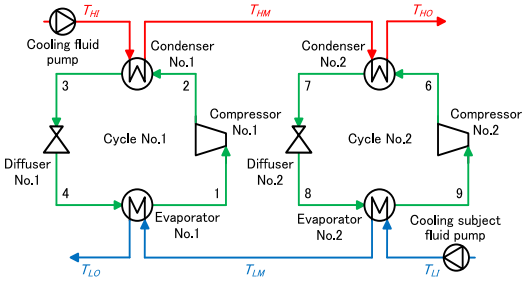

Fig.2 Double-stage Reverse Rankine cycle

3. Calculation Formula

The equations used in this study are shown. The overall coefficient of performance COP and compression power W_P are defined by (1) and (2).

$$COP = \frac{(m_{WF1} \times (h_1 - h_4) + m_{WF2} \times (h_5 - h_8))}{(m_{WF1} \times (h_2 - h_1) + m_{WF2} \times (h_6 - h_5))} \quad (1)$$

$$W_P = W_{P1} + W_{P2} = (m_{WF1} \times (h_2 - h_1) + m_{WF2} \times (h_6 - h_5)) \quad (2)$$

COP represents the performance factor, m_{WF1} and m_{WF2} represent the working fluid flow rate for each cycle. h_1, h_2, and h_4 represent the enthalpies at each point in the cycle No.1, and h_5, h_6, and $h_8$represent the enthalpies at each point in the cycle No.2 ; W_P represents the overall compression power; W_{P1} and W_{P2} are the compression powers for each cycle.

Table 1 Test medium

Name	Classification	Toxicity・flammability
HFC32	Alternative freon	A1
Ammonia	Natural refrigerant	B2L
HFO1233zd(E)	Green refrigerant	A1
HFO1234yf	Green refrigerant	A1
HFO1234ze(E)	Green refrigerant	A2L

Table 2 Calculated conditions

Inlet temperature of Low temperature fluids	0.0[℃]
Outlet temperature of Low temperature fluids	-30.0[℃]
Inlet temperature of High temperature fluids	25.0[℃]
Outlet temperature of High temperature fluids	35.0[℃]
Pressure of Low temperature fluids	101.325[kPa]
Pressure of High temperature fluids	101.325[kPa]
Thermal conductance of Evaporator	（1.8～100）×10^4[W/K]
Thermal conductance of Condenser	（1.8～100）×10^4[W/K]
Refrigeration Capacity	500[kW]

4. Calculation conditions

In this study, air and water were used as low and high temperature heat source, respectively. Table 1 shows the classification of the five refrigerants used in the simulation in terms of composition and the index of toxicity and flammability of the refrigerants defined by ASHRAE. Table 2 shows the simulation conditions: inlet and outlet temperatures of the low and high temperature fluids, thermal conductance and refrigeration capacity of the condenser and evaporator.

5. Calculation Results and Considerations

Figure 3 shows the overall mass flow rate m_{WF} with solid color-coded lines for each refrigerant. In an ove rall charcteristics, it can be seen that the mass flow rate is decreasing with increase of $UA(E)$ in the order of Ammonia, HFC32, and the three HFO refrigerants. In other words, the flow rate required for heat exchange is considered to decrease as the heat dissipation and refrigerating effect increases.

Figure 4 shows the overall compression power W_P with solid color-coded lines for each refrigerant. When the value of HFO1233zd(E), which has the lowest compression power among all refrigerants, is set to 100%, it can be confirmed that the value of each W_P is increased by 1% for Ammonia, by 7% for both HFC32 and HFO1234ze(E), and by 13% for HFO1234yf.

Figure 5 shows the overall coefficient of performance (COP) as a solid color-coded line for each refrigerant.

If the value of HFO1233zd(E), which has the highest COP among all refrigerants, is set to 100%, the COP values are respectively Ammonia decreased by 2%, both HFO1234ze(E) and HFC32 decreased by 7%, and HFO1234yf decreased by 12%, respectively. It can also be confirmed that the ratio difference and order of

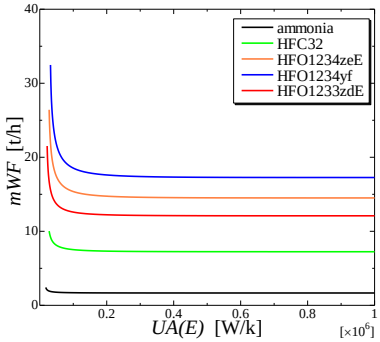

Fig.3 Working fluid flow rate

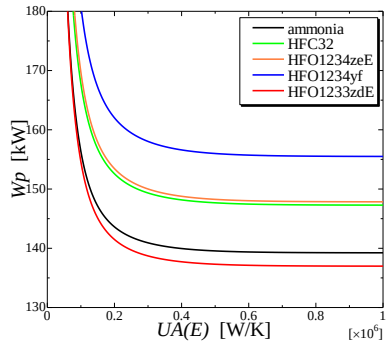

Fig.4 Compression power

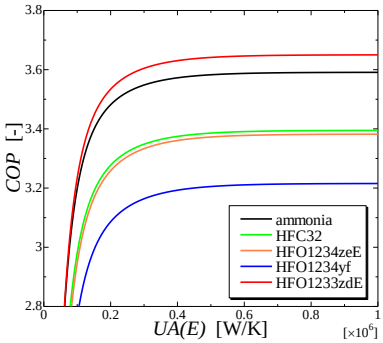

Fig.5 Coefficient of performance

performance is almost the same as that of the compression power W_P.

6. Conclusion

The performance of five refrigerants; three green refrigerants HFOs (HFO1233zd(E), HFO1234yf, and HFO1234ze(E)), Ammonia as a natural refrigerant, and HFC32 as a conventional CFC substitute, were investigated under certain heat source conditions using a double-stage reverse Rankine cycle. HFO1233zd(E) could be operated more efficiently than the other four refrigerants under the present simulation conditions, while in the case of HFO1234yf, it shows lower efficiency overall.

References

(1) Mitsuyo Uno, Approaches to next-generation refrigerant compatibility, Marine Engineering 53 (6), 793-799, 2018-11-01, (2018)

Y. Ikegami, T. Morisaki, Study on heat pump and refrigeration cycle using multi-stage inverted Rankine cycle, Academic paper, Saga Univ. (2013)

Oceanographic Survey for Installation of OTEC Plant in Kumejima Island （Influence from the Aguni Basin）

Shodai NAGATA[1)], Junichi OHARA[1)], Hideyuki YOSHIMURA[1)],
Masaki ARIYOSHI[1)] and Yasuyuki IKEGAMI[2)]

National Fisheries University, 2-7-1 Nagatahonmachi, Shimonoseki-shi, Yamaguchi 759-6595, Japan [1)]
Institute of Ocean Thermal Energy, Saga University, 1-Honjomachi, Saga−shi, Saga 840-8502, Japan[2)]

Abstract

In this study, oceanographic surveys were conducted in the sea area of Kumejima Island, Okinawa Prefecture, which is the best candidate in Japan for the installation of Ocean Thermal Energy Conversion (OTEC), and the surrounding Aguni Basin, and an evaluation was made to clarify whether the seawater in the Kumejima Island sea area is derived from the Aguni Basin. Seawater temperature, salinity, and dissolved oxygen relative to water depth were comparable between the Kumejima Sea area and the Aguni Basin, indicating that the seawater in the Kumejima Sea area is likely to be deep ocean water originating from the Aguni Basin.

Key Words: Oceanographic Survey, Kumejima , Aguni Basin, OTEC, Seawater Temperature

1. Introduction

In October 2020, the Japanese government sat the goal which Japan become carbon neutral country by 2050, and the spread of renewable energy is necessary to achieve this goal. Therefore, this study focuses on ocean thermal energy conversion (OTEC) as a renewable energy source. 70% of the Earth is composed of ocean, and Japan is an island country surrounded by ocean, making it easy to make effective use of ocean energy. OTEC is used not only for power generation, but also for various secondary uses such as air-conditioning, aquaculture, and agriculture[1)].

In this study, oceanographic surveys were conducted in the waters of Kumejima, Okinawa Prefecture, the most promising candidate in Japan for the installation of OTEC, and the surrounding Aguni Basin, and an assessment was made to clarify whether the seawater in Kumejima sea area is derived from the Aguni Basin or not.

2. Ocean Basin

An ocean basin is a flat basin at the bottom of the deep sea, where the seawater temperature is extremely lower as one moves toward the bottom. Deep-sea basins are characterized by the lack of light, the absence of photosynthesis by phytoplankton and other organisms, and the lack of currents, which results in stable levels of nutrients and dissolved oxygen. In addition, when the seawater flows from one ocean basin to other, fixed flows are easily formed due to the characteristics of the topography. If we assume that the seawater which flow from the Aguni Basin to the Kumejima sea area is also fixed in this study, there is a high possibility that the two types of seawater mix and form a unique seawater with similar characteristics[2)].

In order to establish OTEC, it is desirable to have a stable temperature difference of 20°C or more between surface seawater and deep seawater, as well as stable deep seawater with salinity for secondary use of deep seawater, and the endemic seawater in the basin can be said to satisfy these conditions.

3. Period for investigation, survey item, method of water sampling and investigation site

Figure 1 shows the oceanographic survey area. A total of seven sites were surveyed: four in the Kumejima sea area and three in the Aguni Basin.

The electrical conductivity of seawater was measured using a conductivity temperature depth profiler (CTD) aboard the *Koyo Maru* to investigate water depth, seawater temperature, dissolved oxygen, and salinity. The survey was conducted in August 2021.

4. Result and Discussion

4.1 Seawater temperature

Figure 2 shows the results of the vertical distribution of seawater temperature. The results for the Kumejima sea area are shown by the red line, and those for the Aguni Basin are shown by the blue line. Figure 2 shows that there is no difference between the Kumejima sea area and the Aguni Basin, with a rapid decrease from the surface to a depth of around 600 m, followed by a gradual decrease thereafter. The temperature of the seawater at the depth of 900m or deeper is 4 to 5°C.

Therefore, the Kumejima sea area and the Aguni Basin are comparable in terms of seawater temperature,

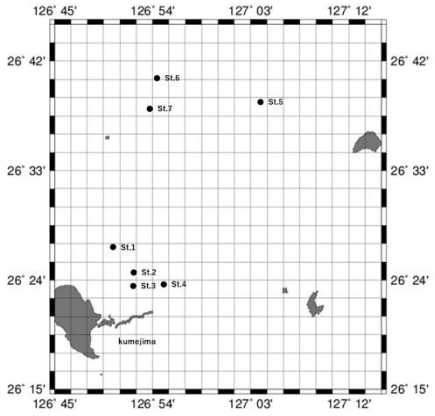

Fig.1 Investigation site

and it is highly likely that the seawater in the Kumejima sea area is fed by stable, low-temperature deep seawater originating from the Aguni Basin. The temperature difference between surface seawater and deep seawater, which is the most important factor in OTEC, can be stably maintained.

4.2 Salinity

Figure 3 shows the results of the vertical distribution of salinity. Salinity is one of the secondary uses of deep seawater used for OTEC and also for aquaculture. The results of the survey in the Kumejima sea area are shown by the red line, and the Aguni Basin is shown by the blue line. Figure 3 shows that there is no difference between the Kumejima sea area and the Aguni Basin, with a rapid increase from the surface to a depth of about 200 m, followed by a rapid decrease to a depth of about 700 m. The salinity increases slowly at depths deeper than 700 m, and then remains stable.

Therefore, as with seawater temperature, the Kumejima sea area and the Aguni Basin are comparable in terms of salinity, indicating that the seawater in the Kumejima sea area is likely to be fed by deep seawater with stable salinity originating from the Aguni Basin, and that stable secondary use of deep seawater is possible.

4.3 Dissolved oxygen

Figure 4 shows the results of the vertical distribution of dissolved oxygen content. Dissolved oxygen is an important parameter for aquaculture. The results of the survey in the Kumejima sea area are shown by the red line, and the Aguni Basin is shown by the blue line. Figure 3 shows that there is almost no difference between the Kumejima sea area and the Aguni Basin, with a gradual decrease from the surface to a depth of around 700 m, followed by a stable transition.

Therefore, the Kumejima sea area and the Aguni Basin are comparable in terms of dissolved oxygen as well as seawater temperature and salinity, and it is highly likely that the seawater in the Kumejima sea area is fed by deep seawater with dissolved oxygen from the Aguni Basin.

5. Conclusions

4) The seawater temperatures in the Kumejima sea area and the Aguni Basin show similar vertical profiles, indicating that the Kumejima sea area is likely fed by cold and stable deep seawater originating from the Aguni Basin.
5) The salinity distribution in the Kumejima sea area and the Aguni Basin is comparable, indicating that the seawater in the Kumejima sea area is likely to be deep seawater with a stable salinity originating from the Aguni Basin.
6) The dissolved oxygen in Kumejima sea area and the Aguni Basin show similar vertical profiles, indicating that the seawater in Kumejima sea area is likely to be deep seawater with dissolved oxygen from the Aguni Basin.

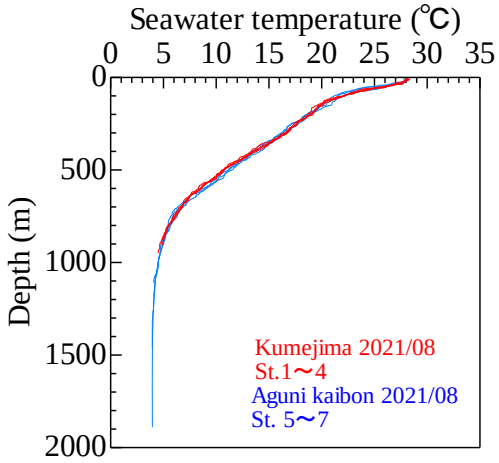

Fig.2 Water temperature vertical distribution

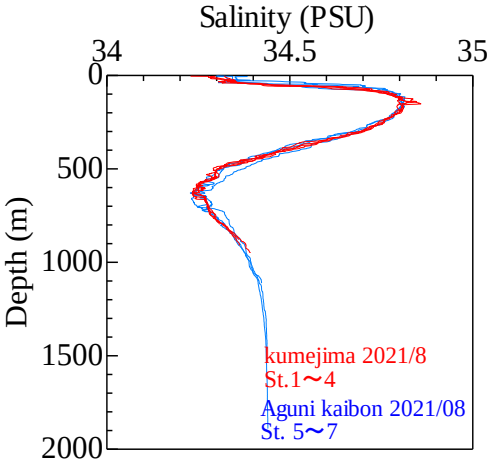

Fig.3 Salinity vertical distribution

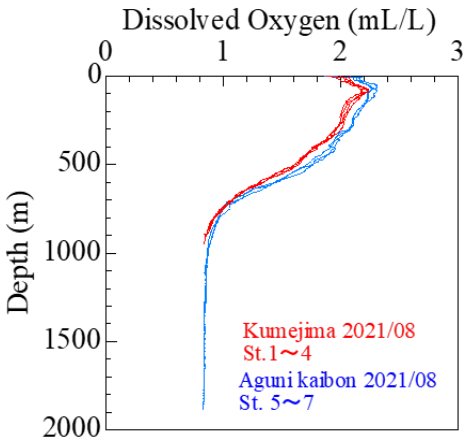

Fig.4 Dissolved Oxygen vertical distribution

References

(1) Yukio NAKAMURA(2017)：Kumejima Island Model Challenging the Cascaded Use of Deep Seawater, Deep Ocean Water Research, Vol.18 No.3 ,210-211
(2) Koshiro TAYA et al.(2022)：Horizontal distribution of the benthic front formed at the boundary between Japan Basin Bottom Water and Yamato Basin Bottom Water in the Japan Sea and modification processes due to mixing of both Bottom Waters, Oceanography in Japan, Vol.31 No.6 ,99-110

・**Title**

「Research on Periodic Characteristics by Visualization of Plate Type Evaporator Interior」

・Authors

Ayano Nakagawa (Saga Univ.)　Ryosuke Nikushi (Saga Univ.)
Takeshi Yasunaga (Saga Univ.)　Takafumi Morisaki (Saga Univ.)
Yasuyuki Ikegami (Saga Univ.)

・Abstract

Plate-type evaporators have been applied to low-source temperature difference power generation because of their high heat transfer performance and compact size. The working fluid in a plate evaporator is a complex gas-liquid two-phase flow with evaporation phenomena, and it is important to understand the internal flow phenomena. However, the unsteady-state void fraction measurement in two-phase flow has not been sufficiently investigated for the observation time. In this research, a herringbone plate evaporator made of transparent resin is used to visualize the evaporation phenomena inside the evaporator to measure the void fraction and to clarify the observation time suitable for the flow conditions.

・Structure of the paper

1. Background
2. Experimental apparatus and method
3. Image processing method
4. Experimental Results and Discussion
5. Conclusion

Development of an Optimization Method for Offshore Jacket Foundation Hosting a Wind Turbine under Static Loads

Takahiro NAGATSU
Institute of Ocean Thermal Energy, Saga University, 1-Honjo machi, Saga shi, Saga 840-8502, Japan
E-mail :23728017@edu.cc.saga-u.ac.jp

Abstract

Wind energy is abundantly available in nature, but due to its low energy density, the size of wind turbines needs to become larger and require vast sites where a large number of wind turbines can be installed in clusters. Therefore, there are high hopes for offshore wind power, where wind resources are abundant and vast sites are available. Offshore wind turbines have so far been developed in Europe and China, where low-cost monopile foundations have been used for the most part. However, as wind turbines become larger and the water depth of the installation area increases, jacket foundations will become increasingly important, as they are easier to ensure strength and rigidity and have fewer restrictions on construction equipment. In particular, the cost of foundations accounts for a large proportion of the cost of offshore wind turbines, so rationalizing the design of jacket foundations is an important issue for reducing the cost of power generation from offshore wind turbines. A jacket foundation basically consists of main structure (four legs) forming the periphery of the platform, and braces connected between the legs.

In this study, an optimization software "JacketDes.m" is developed in Matlab to optimize for the lightest weight of the entire jacket foundation under static wind loads. Overall, five parameters are considered in this optimization study, the diameters and thicknesses of both the main structure and braces of the jacket foundation, and the base width of the four legs. The optimization software "JacketDes.m" controls the calculations of the freeware structural analysis software Frame3DD and uses the results to obtain a lightweight jacket foundation with sufficient resistance to compressive/tensile stresses and buckling. As there are only five parameters in this study, the optimal values are obtained by round-robin method within the pre-defined optimization range for each parameter.

As a demonstration of the optimization method, a case study was conducted, to design the foundation of a 15 MW wind turbine. A four-legged jacket with a deck width 20 m and height 45 m off the coast of northern Kyushu (installation site water depth 20 m) was selected and optimized. As a result, jacket foundations with a base width of 26 m, main structure and brace diameters of 1.2 m and 0.2 m, and respective plate thicknesses of 32 mm and 20 mm were obtained, as the the lightest weighing jacket foundation (1128 t).

The future work includes extending the optimization method to include hydrodynamic forces of waves and currents, seismic loads, terminal and fatigue loads during power generation and welding effects, which are not considered in this study. In the optimization, the development of optimization algorithms for an increased number of parameters, such as higher resolution, individual diameter and thickness settings for each member, topology optimization, etc., should also be considered.

1. INTRODUCTION

This study develops an optimization method for jacket foundations (Fig. 1), which are promising as foundations for very large or deep-water offshore wind turbines.

Fig 1 Example of Jacket Foundation [3]

2. DESIGN METHOD OVERVIEW

In this study, the freeware for 3D frame analysis Frame3DD [1], the optimization software JacketDes.m (newly developed in Matlab) were used to perform the analysis and optimization of the jacket foundations. Here, the bearing capacity is evaluated in terms of compressive/tensile stresses and buckling, and the optimization parameters are the diameters and thicknesses of the main structure and braces, and the base widths. As there are five parameters listed above, the optimum value is obtained by round-robin method within the pre-defined optimization range for each parameter.

The validity of the analysis was verified by the response under known loads.

The ratio of the stress to the allowable values of compressive stress and buckling stress (0.605Et/r; E: Young's modulus, t: plate thickness, r: radius [5]) for each member was taken as effort (ηs, ηb). If these efforts exceed 0.5, the member can be considered to have failed. However, in reality, more loads are applied and there are many conditions that are not assumed in this study. Therefore, in this study, the lightest geometry among those whose effort does not exceed 0.5 is selected as the optimum value.

3. DESIGN

3.1 DESIGN CONDITION

Optimization of a four-leg jacket (deck width 20 m) foundation consisting of SS400 (strength: 400 N/mm2 [4]) cylinders was carried out for an IEA Wind 15 MW Reference Wind Turbine [1] to be installed offshore in

northern Kyushu (base wind speed 34 m/s, roughness category I, water depth 20 m). The design load (at the top of the jacket) was calculated as follows. The design loads (at the top of the jacket) were 16 combinations of 6.1 MN shear force, 634 MNm bending moment, ±39 MNm torque and 18.4 MN axial force from 8 directions.

3.2 DESIGN RESULT

The distribution of effort and mass for a base width of 26 m according to the above conditions and design method is shown in Fig. 2. The optimum shape for this base width is the lightest one with an effort not exceeding 0.5. A similar analysis was carried out for base widths between 20 and 30 m (2 m each) and the results are shown in Fig 3. This determined the following optimum (lightest weight) shapes. The values in brackets are the resolution of each variable.

- Base width : 26 m（2 m）
- Main structure diameter : 1200 mm（200 mm）
  Thickness : 32 mm（2mm）
- Brace diameter : 200 mm（100 mm）
  Thickness : 20 mm（5 mm）
- Mass : 1128 t

4. CONCLUSION

1) An optimization (lightest weight) method for the jacket foundation structure of a land-based offshore wind turbine has been developed.
2) The same design method was applied to a 15 MW Reference Wind Turbine for the IEA Wind Turbine to be installed at a water depth of 20 m off the coast of northern Kyushu, with a base width of 26 m and an optimum geometry of 1128 t. The wind turbine was designed to be installed in the same location as the IEA Wind Turbine.
3) Loads such as during waves and currents, earthquakes and power generation, consideration of fatigue and optimization algorithms are future issues.

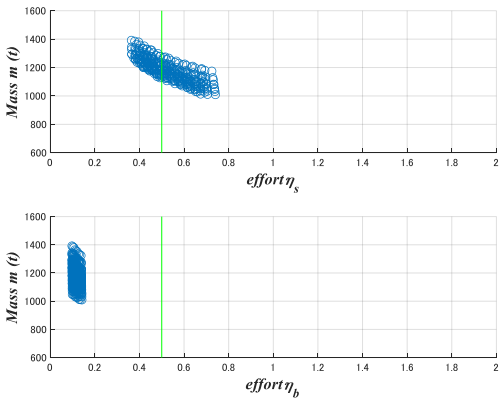

Fig 2 Base Width 22 m Jacket Effort and Mass

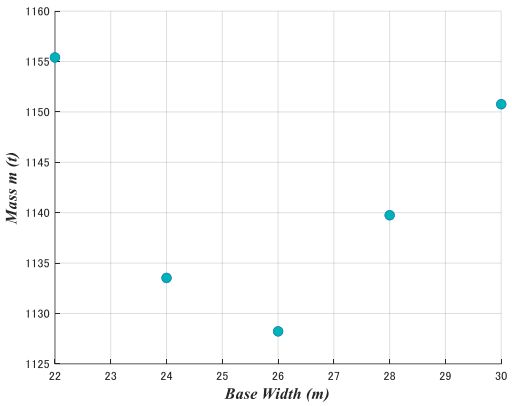

Fig 3 Mass by Base Width

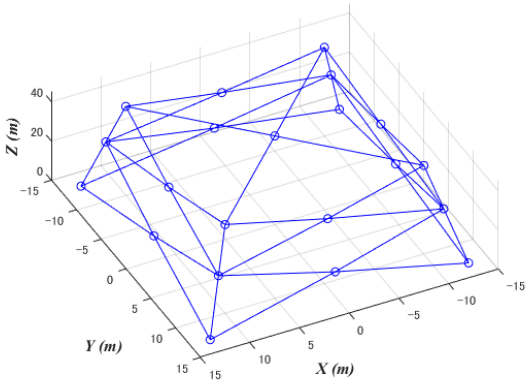

Fig 4 Appearance of The Optimum Jacket Foundation

References

[1] Frame3DD, http://frame3dd.sourceforge.net/
[2] Gaertner, E, et al, Definition of the IEA 15-Megawatt
Offshore Reference Wind, IEA Wind, Technical Report,
2020.
[3] NEDO，着床式洋上風力発電導入ガイドブック（最終版）2018.
[4] JFE , 材料の許容応力度, binran_chapter04.pdf
(jfe-steel.co.jp), Accessed 2023/02/13.
[5] Wind Energy Handbook

Heat transfer characteristics of FCU and plate heat exchanger in seawater air conditioning system

Haruki Ida*, Hirofumi ARIMA**

*Graduate school of Sci. Eng., Saga Univ., 1-Honjo, Saga-shi, Saga 840-8502, Japan

Email: 23728001@edu.cc.saga-u.ac.jp

**Institute of Ocean Energy, Saga Univ., 1-48, Hirao, Kubara-aza, Yamashiro-cho, Imari-shi, Saga, 849-4256, Japan

Abstract

In this study, the air conditioning using seawater was investigated, focusing on the cascade utilization of deep-sea water. The aim of this research that a developing a heat exchanger has optimized performance of a cooling system. Then, the heat transfer performance of the heat exchanger and the seawater cooling system were evaluated. In this experiment, a plate heat exchanger with aluminum plate was employed. In order to evaluate the heat transfer performance at high flow rate conditions, the number of plates was reduced against previous study. In order to evaluate the heat transfer performance of the heat exchanger, a water-water experiment was performed with hot and cold water. Next, in order to evaluate the heat transfer performance of the seawater cooling system with FCU (Fan Coil Unit). In the FCU experiment, cold water and tap water flowed through the heat exchanger and the tap water cooled by the cold water. The cooled water flowed into FCU and heat exchange the cooled water and hot air. The result of these experiments was as follows. As the water-water experiments, the smaller the number of plates in the heat exchanger indicates the larger heat transfer coefficient. As the FCU experiments, it was found that the heat transfer coefficient of the FCU increases with an increase in the mass flow rate of tap water and the flow rate of the air. It was also found that the cooling performance of the cooling system improved at increasing the heat transfer rate of the heat exchanger.

1. Introduction

In this study, the application to the cooling system using deep sea water was paid attention. This cooling system is that indirectly transfers cold heat from deep ocean water using a heat exchanger and an FCU. It is one of the sea water air conditioning system (SWAC). In this study, the heat transfer performance of the heat exchanger and the heat transfer performance of the seawater cooling system were evaluated.

In this presentation, the result of heat transfer characteristics at the higher water flow velocity was reported.

2. Experiment

To evaluate the heat transfer characteristics of the PHE, a water-water experiment and the heat transfer performance of the entire cooling system using the FCU and heat exchanger were performed.

Fig. 2.1 and 2.2 show the schematic diagrams of the water-water experiment apparatus and the FCU experiment apparatus. The water-water experimental apparatus consists of a PHE, a refrigerator, and hot water tank. CU experiment apparatus consists of PHE, a refrigerator, tap water tank, and FCU (Fan Coil Unit). Fig. 2.3 shows that the FCU unit. The equipment of FCU experiment apparatus except of the refrigerator were installed in a storeroom. The inlet temperature of air at the FCU was controlled by an air conditioner.

The material of the PHE test plate is pure aluminum A1050, and the chevron angle is 60°. The experiments were performed using PHE with 5 and 13 plates, in order to compare the heat result of previous research [1] which plate heat exchanger was installed 21 plates.

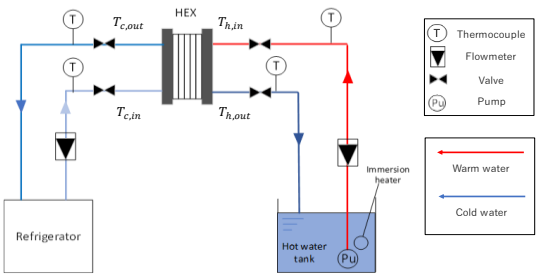

Fig. 2.1 Schematic diagram of water-water experimental apparatus.

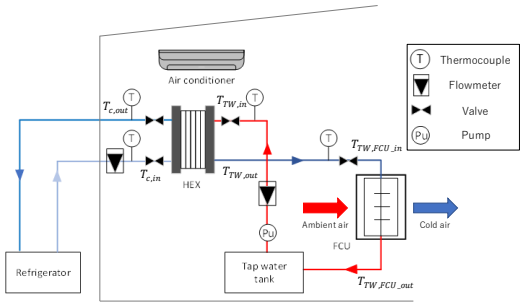

Fig. 2.2 Schematic diagram of FCU experimental apparatus.

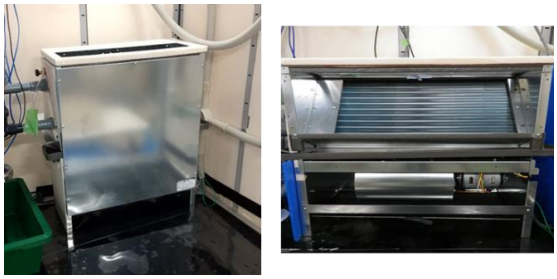

Fig. 2.3 FCU unit

At the water-water experiment, while counter flowing the cold and hot water in the PHE, the investigation the change in heat transfer characteristics due to the difference flow velocity and number of plates were performed.

The experimental conditions were 10°C for cold water and 30°C for hot water.

In the FCU experiment, the hot air and cold tap water was heat exchanged in the FCU., Also, the heat obtained by the FCU is heat exchanged with cold water in the PHE. The air inlet temperature of the FCU was 30°C. Cold water was o 5°C. The flow rate of cold water, tap water, and FCU air were given as experimental conditions. The temperature and flow rate at the inlet and outlet of PHE and FCU were measured.

3. Data reduction

In the water-water experiment and the FCU experiment, the heat transfer rate was calculated by the following equation.

$$U = Q/(A_s \Delta T_{lm}) \quad (1)$$

Q is the heat transfer rate of the heat exchanger, ΔT_{lm} is the logarithmic mean temperature difference, and A_s is the heat transfer area. Each value was obtained by the following equations (2) and (3).

$$Q = mC_p(T_{in} - T_{out}) \tag{2}$$

$$\Delta T_{lm} = \frac{(T_{h,in} - T_{c,out}) - (T_{h,out} - T_{c,in})}{\ln\{(T_{h,in} - T_{c,out})/(T_{h,out} - T_{c,in})\}} \tag{3}$$

where m [kg/s] is the mass flow rate of cold water, C_p [J/(kg · K)] is the specific heat of cold water at constant pressure, $T_{h,in}$, $T_{h,out}$ is the inlet and outlet temperature of the heat exchanger at high temperature side , $T_{c,in}$, $T_{c,out}$ are the inlet and outlet temperatures at the cold temperature side.

The heat transfer coefficient h of the heat exchanger was defined by using the Wilson plot method.

4. Experimental result

4.1 Water-water experiment

Fig. 4.1 shows the correlation between Nu_h and Re_h obtained from the heat transfer coefficient on the hot water side at the different number of plates heat exchanger. Table 4.1 shows the Nusselt number at different number of plates. As shown in Fig. 4.1, heat exchanger has smaller the number of plates indicates high Nu_h.

The cause is considered that the influence of the flow distribution in each channel. As the number of plates increases, the water flow velocity in the channel which is furthest from the entrance becomes slower than near the entrance due to the pressure loss.

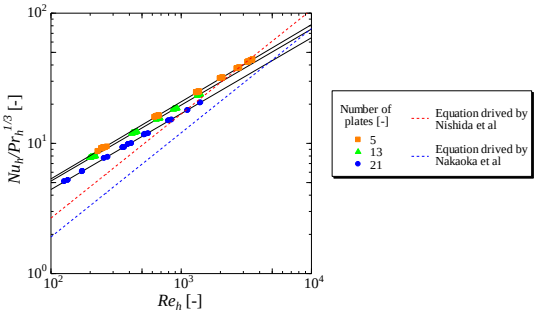

Fig. 4.1 Correlation between Nu_h and Re_h

Table 4.1 Nu_h number

5 plates	$Nu_h = 0.349Re_h^{0.592}Pr_h^{1/3}$
13 plates	$Nu_h = 0.349Re_h^{0.584}Pr_h^{1/3}$
21 plates	$Nu_h = 0.302Re_h^{0.583}Pr_h^{1/3}$

4.2 FCU experiment

Fig. 4.2 shows that the relationship between the mass flow rate G_{tw} of tap water and the heat transfer coefficient $U_{FCU,tw}$ of the FCU, and Fig. 4.3 shows that the comparing the cooling performance at the difference in the heat transfer coefficient of the PHE. In addition, the temperature difference dT_{air} [°C] was calculated by Eq. (4) using the inlet and outlet temperatures on the air side of the FCU.

$$dT_{air} = T_{air-FCU,in} - T_{air-FCU,out} \tag{4}$$

Fig. 4.2 shows that the $U_{FCU,tw}$ increases with an increasing in G_{tw}. Although, the heat transfer coefficient decreased at the highest flow velocity. It is considerd that one possible reason is that the value of the heat transfer coefficient and overall heat transfer coefficient become constant in the region where the flow velocity is high. Also, in Fig. 4.3, it was found that the cooling performance improves with an increases in$U_{tw,PHE}$.

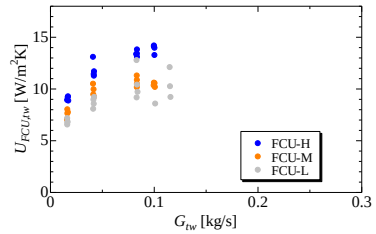

(a) 5 plates

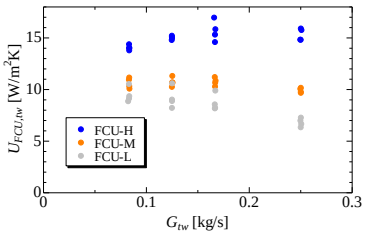

(b) 13 plates

Fig. 4.2 Correlation between mass flow rate G_{tw} and overall heat transfer coefficient $U_{FCU,tw}$.

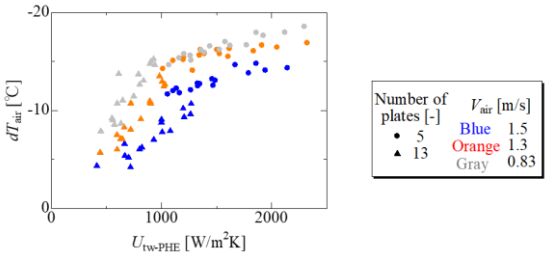

Fig. 4.3 Cooling performance against heat transfer rate of PHE.

5. Conclusion

At the plate heat exchangers with different numbers of plates, the heat transfer performance of the heat exchanger was evaluated and the heat transfer performance of the seawater cooling system installed the heat exchanger. At the reducing the number of plates in the plate heat exchanger against the previous research, the heat transfer characteristics of the fluid in the heat exchanger were investigated under higher flow velocity conditions.

In water-water experiments, it was found that the smaller the number of plates, the higher the heat transfer coefficient. The cause is that the influence of distribution of flow velocity in each channel in plate heat exchanger.

In the FCU experiment, it was found that the heat transfer coefficient on the FCU side increased with an increasing in the tap water flow rate under each number of plates condition. However, the heat transfer coefficient decreased under the condition of the highest flow velocity., It is considered due to the improvement in heat transfer due to the increase in flow velocity exceeded the peak point. Regarding the cooling performance, it was found that the higher the overall heat transfer coefficient of the heat exchanger, the better the cooling performance. By comparing experiments with two different number of plates, it has a wider distribution of the correlation between the overall heat transfer coefficient and the air temperature difference in the FCU.

References

(1) Nishiguchi M., Master's thesis, Graduate School of Science and Engineering, Saga University, 2022.

Boiling heat transfer characteristics of ammonia in micro channel and plate heat exchanger

Shoichi Suehiro*, Hirofumi ARIMA**
*Graduate school of Sci. Eng., Saga Univ., 3-hara, Fukuoka-shi, Fukuoka 814-0022, Japan
Email: 23728014@edu.cc.saga-u.ac.jp
** Institute of Ocean Energy, Saga Univ., 1-48, Hirao, Kubara-aza, Yamashiro-cho, Imari-shi, Saga, 849-4256, Japan

Abstract

To improve the performance of the heat exchanger for OTEC, it is necessary to clarify the boiling heat transfer characteristics of ammonia of the heat exchanger. In this study, the effect of the channel shape of heat exchanger and shape of heat transfer surface of PHE were focused, and the overall and the boiling heat transfer coefficient were measured using ammonia as the working fluid on micro channel (MCHE) and plate heat exchanger (PHE). The MCHE has 35 stages with 51 channels per stage. The heat transfer surfaces of PHE has a herringbone surface which were anodized aluminum plates. The anodic oxidation was performed to increase the corrosion resistance for ammonia. As a result, it was clarified that the effect of the mass flow rate and temperature of hot water and on the overall heat transfer coefficient and boiling heat transfer coefficient. Further, an empirical correlation for the boiling heat transfer coefficient based on the Lockhart-Martinelli parameter was derived.

Key Words: Overall heat transfer coefficient, Boiling heat transfer coefficient, MCHE, PHE, Lockhart-Martinelli parameter

1. Introduction

In order to improve the performance of heat exchanger for OTEC, it is essential to clarify the boiling heat transfer characteristics of heat exchanger. The overall heat transfer coefficient and boiling heat transfer coefficient were measured to clarify the boiling heat transfer characteristics on MCHE and PHE. To improve the performance of heat exchangers used in OTEC, various studies have been conducted, such as heat transfer characteristics of ammonia, channel shape of heat exchanger, shape of heat transfer surface of PHE, enhancement boiling heat transfer coefficient, Pressure drop and material of heat transfer surface. Therefore, in this study, MCHE was investigated the effect of channel shape of heat exchanger. In addition, PHE was investigated the effect of shape of heat transfer surface.

2. Experiment

2.1 Experimental apparatus

Fig. 1 shows that the schematic diagram of experimental apparatus. The experimental apparatus consists of a heat exchanger, a refrigerator 1 and 2, a subcooler, a hot water tank, a hot water pump and a working fluid tank. The ammonia is used as the working fluid. The MCHE and PHE has been adopted as a heat exchange. The quantity of state which measured by each sensor are collected and recorded in a data logger. In addition, the experimental apparatus has three circulation cycles: a working fluid, a cold water and a hot water circulation cycle.

Fig. 2 shows that an external view of the MCHE which is made of SUS316. The size of MCHE is width of 140 mm × length of 200 mm × thickness of 40 mm. The MCHE has 35 stages with 51 channels per stage.

Fig. 3 shows that an external view of test plate which is made of A1050 for PHE. The size of PHE is width of 100 mm × length of 350 mm × thickness of 1 mm. The surface shape of the plate is herringbone and the chevron angle is 60 degrees. This test plate is surface-treated by anodic oxidation specified in JIS H8601 in order to provide corrosion resistance.

Table 1 and 2 show that the experimental conditions of this experiment in MCHE and PHE.

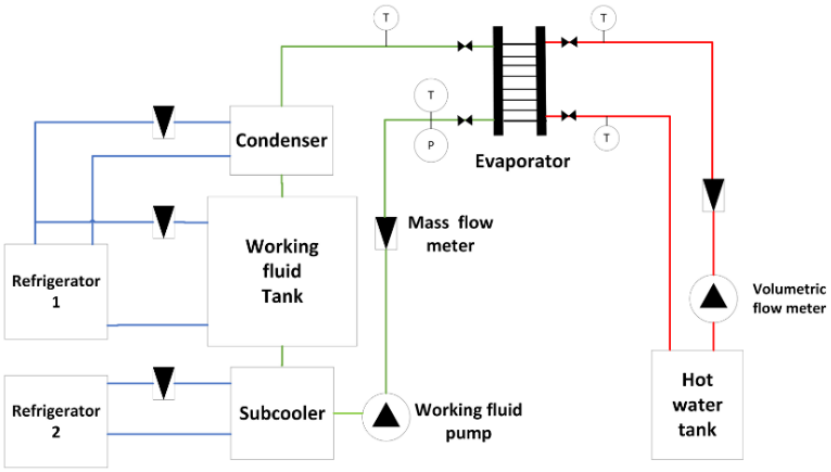

Fig. 1 Schematic diagram of experimental apparatus.

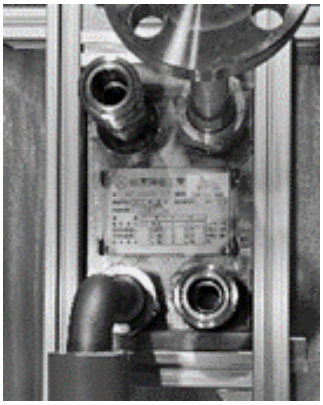
Fig. 2 MCHE

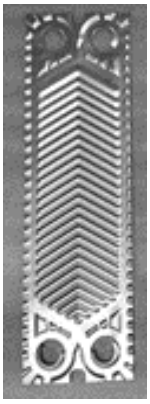
Fig. 3 PHE

Table 1 Experimental conditions (MCHE).

Pressure [kPa]	700
Mass flow flux of working [kg/m^{2}s]	8.2, 10.2, 12.3, 14.3
Flow rate of hot water [L/min]	1, 2, 3, 4, 5
Inlet temperature of hot water [°C]	25,30,35,40

Table 2 Experimental conditions (PHE).

Pressure [kPa]	700
Mass flow flux of working [kg/m^{2}s]	2.7, 3.9, 5.8, 7.7, 11.6
Flow rate of hot water [L/min]	1, 2, 3, 4, 5
Inlet temperature of hot water [°C]	25, 30, 40

2.2 Data reduction

The overall heat transfer coefficient U and boiling heat transfer coefficient h_{wf} were obtained by the experimental data. These values were calculated by following equations:

$$U = Q_h/(A_S \Delta T_{lm}) \tag{1}$$

$$\frac{1}{h_{wf}} = \frac{1}{U} - \left(\frac{1}{h_h} + \frac{t}{k}\right) \tag{2}$$

Further, heat transfer of hot water h_h was calculated by a following equation proposed by Nishiguchi[(1)].

$$Nu = h_h D_{eq}/k_h = C_1 Re^n Pr^{1/3} \tag{3}$$

where $C_1 = 0.4, n = 0.23$ at MCHE and $C_1 = 0.31, n = 0.58$ at PHE (Nishiguchi[(1)]).

3. Result and discussion

3.1 Overall heat transfer coefficient

Fig 4 (a) and (b) show that the overall heat transfer coefficient U (at $T_{h,in} = 30℃$) of in MCHE and PHE. At the result of the MCHE in Fig. 4 (a), the overall heat transfer coefficient tends to increase with an increase in hot water velocity at hot water velocity V_h < 0.1. However, it remains almost constant at V_h > 0.1.

At the result of the PHE in Fig. 4 (b), the overall heat transfer coefficient tends to increase at V_h < 0.2. However, in case of V_h > 0.2, it remains almost constant at the large mass flow flux G of working fluid.

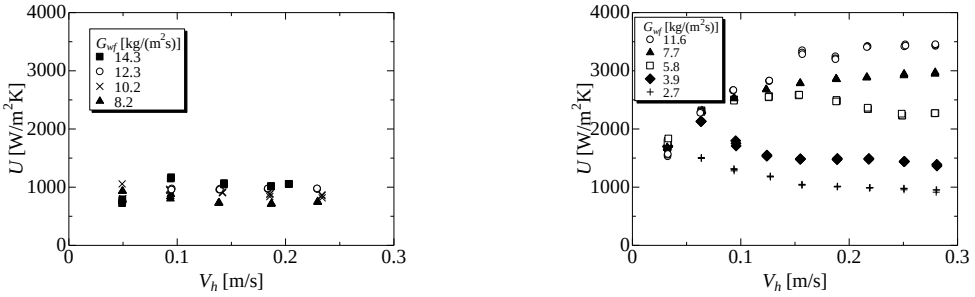

(a) MCHE, $T_{h,in} = 30℃$ (b) PHE, $T_{h,in} = 30℃$

Fig. 4 Overall heat transfer coefficient against hot water velocity.

3.2 Boiling heat transfer coefficient

Fig 5 (a) and (b) show that the boiling heat transfer coefficient h_{wf} (at $T_{h,in} = 30℃$) in MCHE and PHE. According to Fig. 5 (a) and (b), the boiling heat transfer coefficient tends to increase at vapor quality x < 0.4. However, it decreases at x > 0.4.

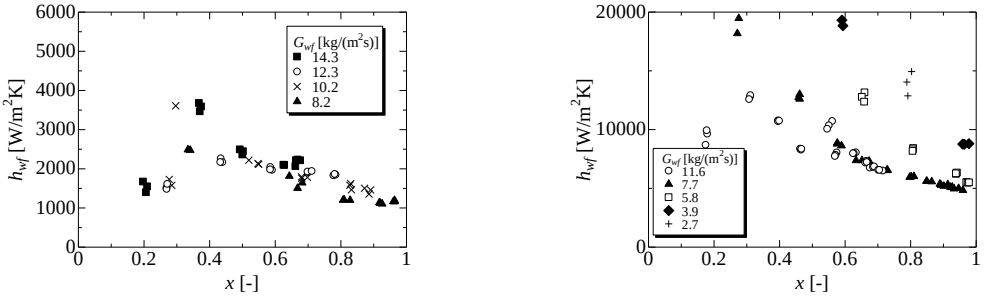

(a) MCHE, $T_{h,in} = 30℃$ (b) PHE, $T_{h,in} = 30℃$

Fig. 5 Boiling heat transfer coefficient against quality.

3.3 h_{wf}/h_{LZ} as a function of $1/X_{vv}$

Fig 6 (a) and (b) show that the relationship between the ratio h_{wf}/h_{LZ} and $1/X_{vv}$ at MCHE and PHE. Lockhart-Martinelli parameter X_{vv} and h_{LZ} was calculated by following equations:

$$X_{vv} = \{(1-x)/x\}^{0.5}\left(\rho_g/\rho_l\right)^{0.5}\left(\mu_l/\mu_g\right)^{0.5} \quad (4)$$

$$h_{LZ} = 0.23\frac{k_l}{D_{eq}}\left[\frac{G(1-x)D_{eq}}{\mu_l}\right]^{0.8} Pr_l^{0.4} \quad (5)$$

The derived correlation of MCHE and PHE with Lockhart-Martinelli parameter are as follows:

[MCHE] $h_{wf}/h_{LZ} = 3.3(1/\mathrm{X}_{vv})^{0.80}$ (6)

[PHE] $h_{wf}/h_{LZ} = 22.6(1/\mathrm{X}_{vv})^{0.97}$ (7)

On the other hand, the correlation equation of Arima et al. [2] which is correlation for flat plate are as follows:

$h_{wf}/h_{LZ} = 16.4(1/\mathrm{X}_{vv})^{1.08}$ (8)

According to Fig. 6 (a), the correlation of Lockhart-Martinelli parameter for MCHE is lower than the correlation of Arima et al. [2] However, in case of PHE, the value of present study is larger than the correlation.

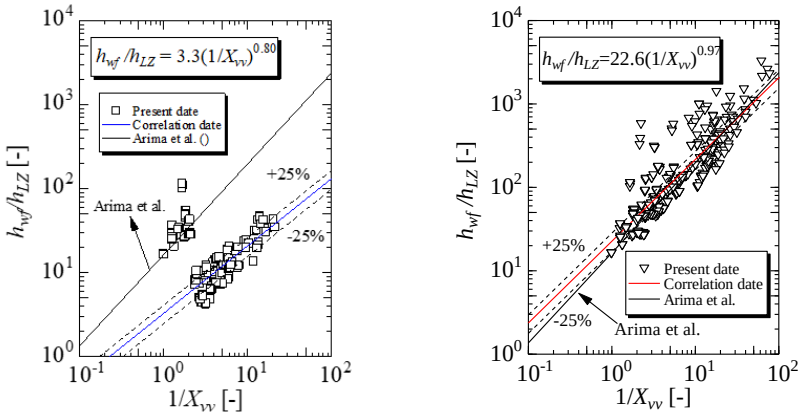

(a) MCHE (b) PHE

Fig. 6 h_{wf}/h_{LZ} as a function of $1/X_{vv}$

4. Conclusion

(1) At the MCHE, the overall heat transfer coefficient tends to increase with an increase in hot water velocity at hot water velocity V_h < 0.1. However, it remains almost constant at V_h > 0.1.
At PHE, the overall heat transfer coefficient tends to increase at V_h < 0.2. However, in case of V_h > 0.2, it remains almost constant at the large mass flow flux G of working fluid.

(2) At the MCHE and PHE, the boiling heat transfer coefficient tends to increase at vapor quality x < 0.4. However, it decreases at x > 0.4.

(3) The correlation of Lockhart-Martinelli parameter for MCHE is lower than the that of Arima et al. However, that of PHE is large than the that of Arima et al. [2].

5. References

(1) Nishiguchi M., Master's thesis, Graduate School of Science and Engineering, Saga University, 2022.

(2) H. Arima, J. H. Kim, A. Okamoto, Y. Ikegami, “Local boiling heat transfer characteristics of ammonia in a vertical plate evaporator”, International Journal of Refrigeration, Vol. 33, No. 2 (2010), pp. 359-370.

Research on optimal design of ocean thermal energy conversion system

Takayuki HARAGUCHI, Takafumi MORISAKI, Takeshi YASUNAGA and Yasuyuki IKEGAMI
Institute of Ocean Thermal Energy, Saga University, 1-Honjo machi, Saga shi, Saga 840-8502, Japan
E-mail :23728018@edu.cc.saga-u.ac.jp

Abstract

Since ocean thermal energy conversion (OTEC) uses the temperature difference of about 20°C in seawater to generate electricity, the available temperature difference is very small compared to thermal power generation method. In order to promote practical use, it is important to design with consideration for higher performance and installation requirements. In this paper, we focused on the optimization of the OTEC system under the conditions of the set Deep ocean water (DOW) discharge, targeting the combined use of heat and seawater resources such as the Kumejima model. We clarified the characteristics of each objective function of conventional optimization, along with the optimum Surface ocean water (SOW) flow rate at a set DOW flow rate. As a result, in the multi-stage use of DOW, the optimization of OTEC when the DOW flow rate is set was examined, and the relationship between the SOW flow rate and the conventional objective function was clarified. Furthermore, as a theoretical study when the DOW flow rate is set, an estimation formula for C_H that maximizes the net power for C_L was derived by numerical analysis.

1. Introduction

Since ocean thermal energy conversion (OTEC) uses the temperature difference of about 20°C in seawater to generate electricity, the available temperature difference is very small compared to other power generation methods. In other words, theoretically, the amount of heat required for the work of the heat engine is large, and the heat transfer area of the heat exchanger is large. Therefore, in order to promote practical use, it is important to design with consideration for further performance and installation requirements. Heat exchanger occupies the largest volume in the total volume of the floating body, and since titanium is used as the material, the heat exchanger is the component that has the greatest impact on the construction cost. Therefore, in the design of the OTEC power plant, minimization of the construction cost is simply calculated by assigning it to the optimization with the ratio of the total heat transfer area of the heat exchanger per net power as the objective function [1].

On the other hand, it is estimated that water intake facilities account for about 70% of the total installation cost for a small-scale (1~5MW) land-based OTEC. Above all, the cost of intake equipment for DOW accounts for 80% of the installation cost [2]. For the purpose of reducing the installation cost of water intake equipment, attempts have been made to design single-stage Rankine cycle (S-R) and two-stage Rankine cycle (D-R) to minimize the total amount of seawater intake. Furthermore, in order to reduce the DOW water intake, an optimization method was constructed to minimize the DOW water intake [3]. However, results have been obtained by optimization, but the Reynolds number is high, and an empirical formula for the heat transfer coefficient at a high Reynolds number is required in order to improve the accuracy of the optimization.

In addition, combined use of DOW including OTEC is expected as a Kumejima model. If the main purpose is to use DOW like the Kumejima model, it is important to optimize the OTEC system under the set DOW flow rate. There are not many studies of OTEC optimization in such cases.

Therefore, in this research, with the aim of optimizing the OTEC system with a constant DOW flow rate, we clarified the characteristics of each objective function along with the optimal SOW flow rate under this condition. For this optimal design, we conducted experiments in a wider range than the conventional applicable range for the heat transfer equation of the Cross flow plate heat exchanger to be used, and derived a new estimation equation. Furthermore, as a theoretical study when the DOW flow rate is set, the optimum SOW flow rate estimation formula is examined by numerical analysis.

2. Evaporator performance test

In the experiment, a performance test was conducted on a cross-flow plate heat exchanger using a 15kW OTEC experimental apparatus. Schematic diagram of the OTEC system using Rankine cycle is shown in Fig.1. This system consists of an evaporator, a working fluid pump, piping, a turbine, a condenser, a separator, and a generator.

The experimental conditions were a hot water temperature of 29°C, a cold water temperature of 9°C, a hot water flow rate of 120-390 m^3/h, and a vapor quality of the working fluid at the evaporator outlet of about 0.8. Pure ammonia was used as the working fluid. In this study, in order to extend the application range, the current study was conducted at 1400 to 4500, compared to Re = 1400 to 2500 in conventional experimental condition.

From the experimental results, Nu_{WS} on the hot water side obtained the following estimation formula.

$$Nu_{WS} = 0.0858 Re_{WS}^{0.8} Pr_{WS}^{1/3}$$

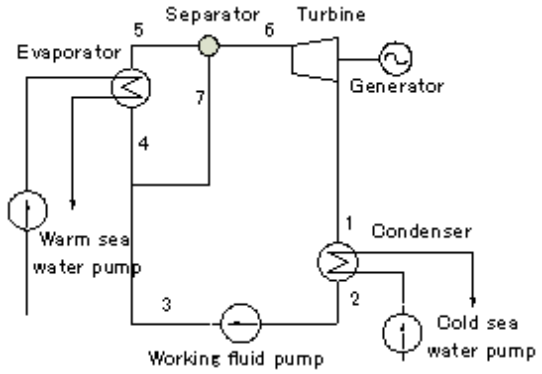

Fig.1 Rankine Cycle

3. Evaluation of the objective function when the amount of DOW intake is constant

In this study, the OTEC system was optimized for the DOW flow rate, assuming that the power generation output of the OTEC is determined from the set DOW flow rate when the OTEC is installed mainly for the purpose of multi-stage use of the DOW. In this optimal design, the following objective function $\gamma_1, \gamma_2, \gamma_3$, which has been used conventionally, was used.

$$\gamma_1 = (A_{Esum} + A_{Csum})/W_{net}$$
$$\gamma_2 = (A_{Esum} + A_{Csum})W_{max}\ /W_{net}$$
$$\gamma_3 = (A_{Esum} + A_{Csum})m_{cs}/W_{net}$$

where γ_1 is the total heat transfer area per net power, γ_2 is the total heat transfer area for the exergy efficiency, and γ_3 is the objective function for reducing DOW water intake.

The optimum design was performed using the heat balance, the performance of each component, and the empirical formulae for convective heat transfer coefficient. Fig.2 shows the relationship between the SOW flow rate $Q_{V,L}$ and each objective function when the DOW flow rate $Q_{V,H}$ = 10000m^3/h and the DOW intake pipe length is 1000m. Fig. 3 shows the relationship between the change in γ_1 and the net power when the intake pipe length and DOW flow rate are changed.

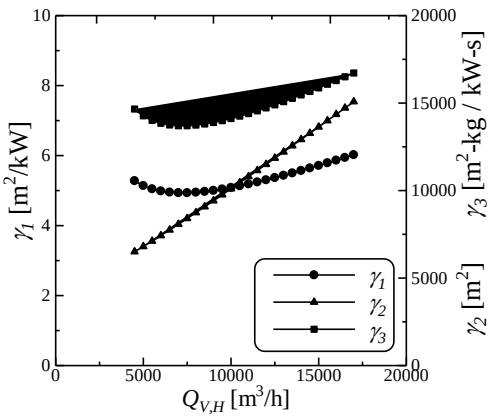

Fig. 2 Relationship between $Q_{V,H}$ and $\gamma_1, \gamma_2, \gamma_3$

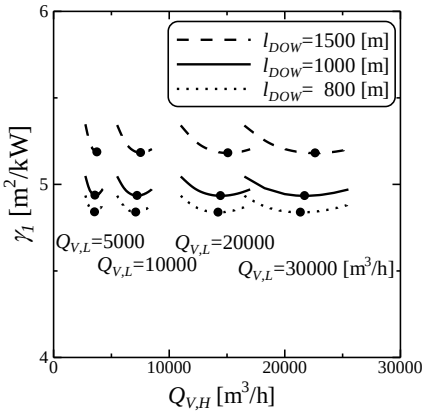

Fig. 3 Relationship between $Q_{V,H}$ and γ_1

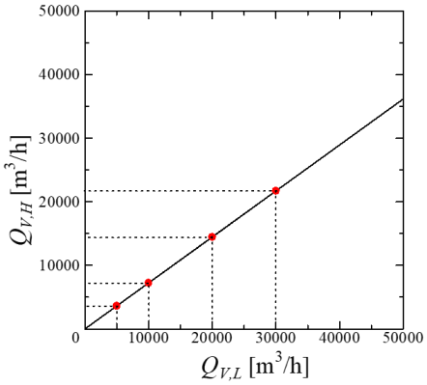

Fig. 4 Relationship between $Q_{V,L}$ and $Q_{V,L}$ at the optimum point (l_{DOW} = 1000m)

From Fig.2, we confirmed that γ_1 and γ_3 are minimized, and γ_2 decreases as the SOW flow rate decreases. From the figure, it was clarified that there exists an optimum SOW flow rate for the set DOW flow rate at γ_1 and γ_3. It was also confirmed that the optimum conditions are equivalent under the constant DOW flow rate. From Fig.3, it was confirmed that the minimum value of the objective function takes the same value for each intake pipe length.

Also, looking at the flow rate at this optimum point, it was newly found that the SOW flow rate relative to the DOW flow rate is determined for each OTEC design condition. Fig. 4 shows the relationship between the DOW flow rate and the SOW flow rate when the length of the DOW intake pipe is 1000m. Clearly, the optimum SOW flow rate is determined by the DOW flow rate.

4. Theoretical study for constant DOW flow rate

In this study, numerical analysis was conducted to find the theoretical formula for the SOW flow rate that maximizes the net power under the condition that the DOW flow rate is set. Equation (2) is the relational expression of the net power by Ikegami et al. [4]. The derivative of Eq.(2) is Eq.(3), and the relational expressions of the heat capacity flows C_H and C_H that satisfy Eq.(3) are derived.

$$W_{net} = \Delta T(C_H^{-1} + C_L^{-1})^{-1} - R_H C_H^{n+1} - R_L C_L^{n+1} \quad (2)$$

$$\left(\Delta T = \left(\sqrt{T_H} - \sqrt{T_L}\right)^2\right)$$

$$\frac{\partial W_{net}}{\partial C_H} = \frac{\Delta T}{(C_H^{-1} + C_L^{-1})^2} - (n+1)R_H C_H^{n+2} = 0 \quad (3)$$

Here, DOW temperature $T_L = 4$ ℃, SOW temperature $T_H = 28$ ℃, $n = 1.8$, flow resistance variable $R_L = R_H = 10^{-7}$ K$^{2.8}$/MW$^{1.8}$, Fig. 5 shows the relationship between C_H and W_{net} when $C_L = 1000$ MW/K, and Fig. 6 shows the relationship between C_L and $C_{H,OPT}$.

From Fig. 5, it can be confirmed that the optimum value of C_H that maximizes the net power ($W_{net,MAX}$) with respect to C_L can be obtained. Fig. 6 shows the relationship of $C_{H,OPT}$ to changes in C_L under the same conditions of n, $\Delta T$and R_H. From this relationship, n, ΔT and R_H are variables, and the optimal relational expression of $C_{H,OPT}$ for C_L is derived as shown in Equation (4). Table 1 shows the conditions under which Eq. (4) holds. In addition, Fig. 7 shows the theoretical formula for obtaining the optimum value of C_H, and the relationship between the optimum values of C_H in Eqs. (3) and (4).

$$C_{H,OPT} = 4.15n^{-1.68}\Delta T^{0.249}R_H^{-0.250}C_L^{0.682n^{-0.928}} \quad (4)$$

From Fig.7, we confirmed that the error of Equation (4) derived by numerical analysis is within ±10%.

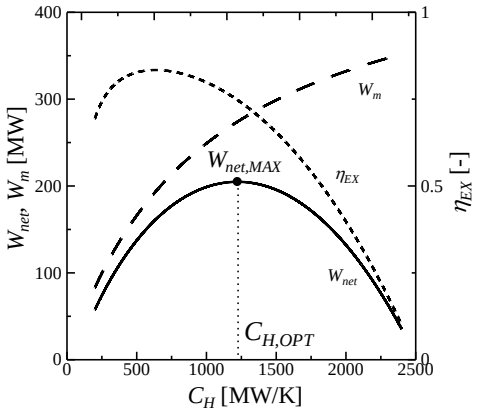

Fig. 5 Relationship between $C_H$and W_{net}

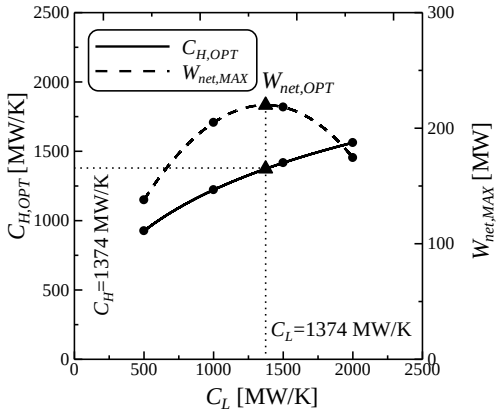

Fig. 6 Relationship between C_L, and $C_{H,OPT}$

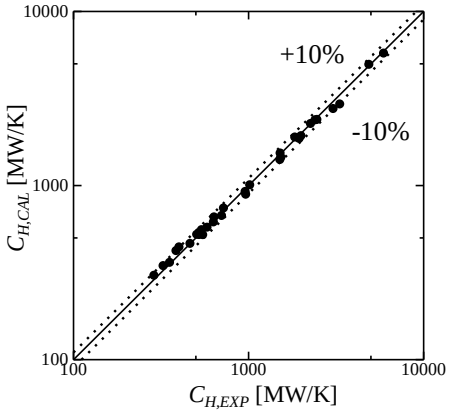

Fig. 7 Relationship between $C_{H,EXP}$ and $C_{H,CAL}$

Table 1 Range in equation (4)

$1.5 \le n \le 2.0$
$0.3 \le \Delta T \le 1.0$
$1 \times 10^{-7} \le R_H \le 4 \times 10^{-7}$
When $W_{net} > 0$, $C_L < 44.2n^{-8.06}R_H^{-0.576}\Delta T^{\frac{1}{n}}$

5. Conclusions

In the multi-stage use of DOW, the optimization of OTEC when the DOW flow rate was investigated. Regarding the relationship between the SOW flow rate and the conventional objective function, it was clarified that the optimum SOW flow rate exists for the set DOW flow rate in γ_1 and γ_3, and that these objective functions can be optimized. In addition, it was clarified that the optimum SOW flow rate was determined when the DOW flow rate was determined for each OTEC design condition. Furthermore, an estimation formula for C_H that maximizes the net power for C_L was derived by numerical analysis, and it was confirmed that the error of this estimation formula was within ±10%.

References

[1]上原，中岡，機論(B 編)，50-456(1984)，pp.1955-1962

[2]沖縄県久米島町，久米島海洋深層水複合利用調査報告書，(2011)

[3]中村泰誠，”陸上型海洋温度差発電の最適設計法の構築に関する研究”，令和 3 年度　修士論文,pp.1-141

[4] Y. Ikegami, et al., J. Sol. Energy Eng, 120(1998),pp. 139-144

Experimental study of a hybrid hot spring water temperature difference power generation system

Tomoyuki HIRAISHI, Takahumi MORISAKI, Naoki NAKAZIMA Yasuyuki IKEGAMI
Institute of Ocean Thermal Energy, Saga University, 1-Honjo machi, Saga shi, Saga 840-8502, Japan
Tel :+81-0952-28-8624, FAX : +81-0952-28-8595, E-mail :23728019@edu.cc.saga-u.ac.jp

Abstract

Japan has about 10% of the world's active volcanoes [(1)] and possesses a large geothermal potential. Among these, small-scale binary power generation is expected to be one of the most promising, but adhesion to pipes and heat exchangers is an issue. As a countermeasure, hybrid hot spring water temperature difference power generation (H-STEC), which uses flash evaporation of hot spring water, has been proposed. This study aims to clarify the characteristics of the H-STEC power generation system and its effect on the working fluid flow rate. It is found that the upper limit of the working fluid flow rate exists under the operating conditions of this H-STEC system because the superheat at the turbine inlet is determined by the working fluid flow rate due to the constant evaporation temperature of the hot spring water. In the future, we will experimentally clarify the characteristics of this system when it is applied using R1224yd, a low-GWP refrigerant.

Key Words: Flash evaporation, H-STEC, Hot spring, Maximum power, Self-supplied water system

1. INTRODUCTION

Japan has approximately 10% of the world's active volcanoes [(1)], and as one of the world's largest volcanic countries, it possesses a large amount of geothermal potential. Japan has the world's third largest geothermal potential, with a geothermal resource of approximately 23.47 million kW [(2)]. In fact, Japan's geothermal power plants have an approved output of 603 MW (in 2021) [(3)].

In addition, geothermal power generation is not affected by weather conditions, and stable power generation is possible day and night because power is generated by pumping up steam and hot water from geothermal reservoirs deep underground. Therefore, geothermal power generation has a high utilization rate among renewable energies, with a facility utilization rate of 56% compared to 13% for solar power and 20% for wind power [(4)]. In Japan in particular, geothermal water with low temperatures is scattered throughout the country.

Figure 1 shows a schematic diagram of a binary power generation system. Binary power generation uses an organic Rankine cycle (ORC), in which a geothermal fluid with a relatively low temperature of 150°C or lower is used as a heat source to exchange heat with a low-boiling-point medium that has a lower boiling point than water. Because the low-boiling medium is used as the working fluid, binary power generation can generate power using heat at medium to low temperatures, which is not possible with the flash method. It also has the advantage of a large pressure difference before and after the turbine, which allows the turbine to be downsized. However, the heat transfer performance is degraded when silica, calcium carbonate, and other components in the geothermal fluid adhere to the heat exchanger as scale, causing a reduction in power generation output. In addition, if an air-cooled condenser is used, it is larger than a water-cooled condenser, and if a water-cooled condenser is used, securing water resources is an issue.

This study focuses on a hybrid hot spring water temperature difference power generation system: H-STEC, which combines a flash evaporation system and a hot spring water temperature difference power generation system.

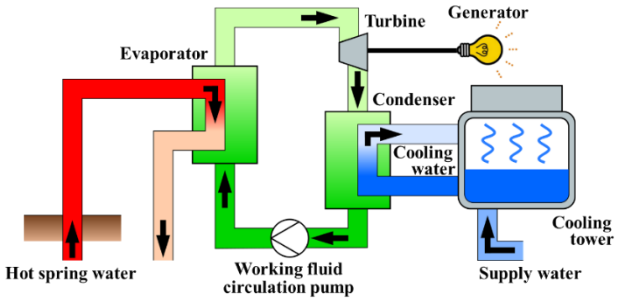

Fig.1 General STEC system (hot spring binary power generation)

Conventional studies on H-STEC have not experimentally clarified the operational and essential cycle characteristics to obtain the maximum power output of H-STEC, especially the cycle characteristics including working fluid and turbine inlet superheat. This study experimentally clarifies the optimum operating conditions for H-STEC in terms of working fluid flow rate and turbine inlet superheat.

Silica and calcium carbonate components dissolved in the hot spring water precipitate and adhere to the heat exchanger, resulting in a decrease in the flow rate of the hot spring water and a decrease in the amount of heat that can be recovered by the heat exchanger. As a result, it has been reported that the power output decreases with continued operation [(5)]. Although many studies have been conducted on anti-scale measures, they have yet to reach a satisfactory solution.

In the case of an air-cooled condenser, air is used as the cold heat source, eliminating the need for water resources. However, since the heat transfer coefficient of the air side is lower than that of the working fluid side, a large heat transfer area must be secured by installing fins on the air side, which may make it the largest structure among the components. On the other hand, when using a water-cooled condenser, securing the cooling water required to cool the working fluid is an issue.

This study focuses on a hybrid hot spring water temperature difference power generation system: H-STEC, which combines a flash evaporation system and a

hot spring water temperature difference power generation system.

Conventional studies on H-STEC have not experimentally clarified the operational and essential cycle characteristics to obtain the maximum power output of H-STEC, especially the cycle characteristics including working fluid and turbine inlet superheat.

In addition, the effectiveness of H-STEC in preventing scale deposition in the evaporator by flash evaporation has not been quantitatively evaluated.

In addition, the recent addition of R245fa, a conventionally used working fluid, to the regulatory list has prompted ORC to investigate alternative working fluids, but no evaluation of the applicability of alternative working fluids to H-STEC has been conducted. In this study, the following three points will be investigated.

1. To experimentally clarify the optimum operating conditions for H-STEC in terms of working fluid flow rate and turbine inlet superheat.

2. To quantitatively clarify the scale deposition prevention effect of H-STEC in the evaporator by chemical analysis of hot spring water and condensate.

3. Apply R1224yd, a low-GWP refrigerant proposed as an alternative to R245fa, as well as R245fa, to H-STEC to theoretically clarify the characteristics inside the cycle and to clarify the applicability and validity of the alternative working fluid.

2. ANALYSIS

The specifications of the flash chamber used in the experiment and photographs of its exterior are shown in Fig. 2, respectively. The flash chamber has one nozzle connected to the hot spring water inlet, and flash evaporation occurs when the water leaves the nozzle. The generated vapor is sent to the evaporator through a demister. The evaporator has a connection to a vacuum pump, and the internal pressure can be changed by opening a valve.

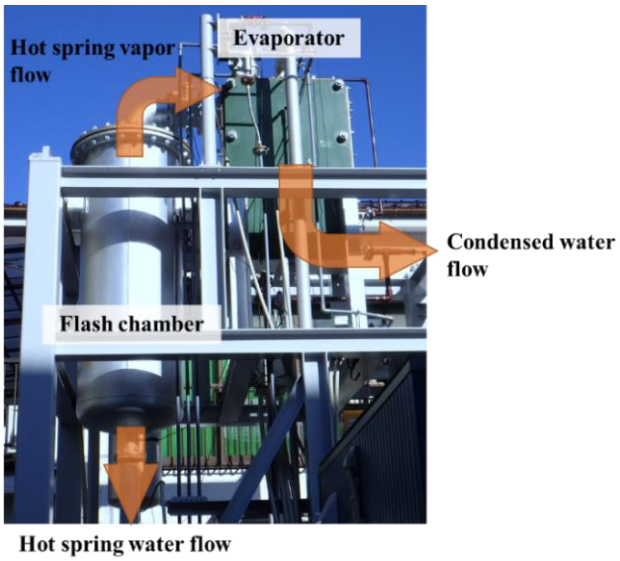

Fig.2 Hot spring steam and condensate flow

3. Result and Consideration of Calculation at cycle

Fig. 3 shows the relationship between the working fluid flow rate and the evaporation and condensation pressures. The evaporation pressure is increasing in relation to the working fluid flow rate, and the differential pressure at the turbine inlet and outlet is increasing.

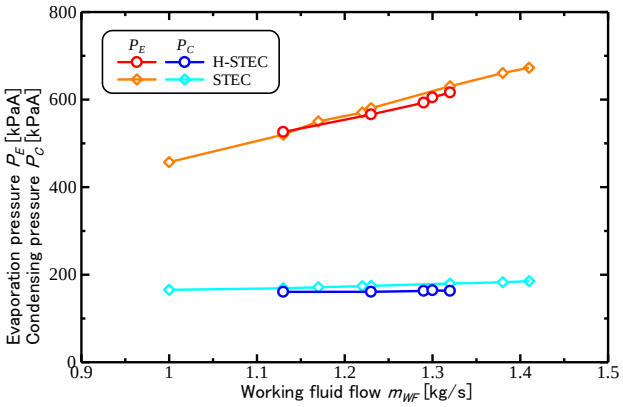

Fig.3 Evaporation and condensation pressures versus working fluid flow rate

Fig. 4 shows the relationship between the working fluid flow rate and the power generation end output with the refrigerant R245fa. The increase in the differential pressure between the turbine inlet and outlet with the increase in the working fluid flow rate is a factor. On the other hand, the turbine inlet superheat, $\triangle T_{TIsh}$, showed a decreasing trend. This is thought to be due to the lower heat source available for H-STEC compared to STEC.

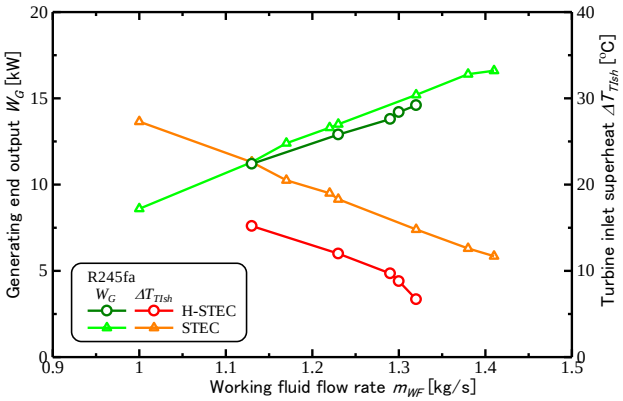

Fig.4 Generating end power and turbine inlet superheat versus working fluid flow rate.

Fig. 5 shows the relationship between the working fluid flow rate and the cycle thermal efficiency. The cycle thermal efficiency and the maximum power ratio are increasing for both STEC and H-STEC. In this case, the cycle thermal efficiency is increasing because the output is increasing and the rate of increase of the heat exchanged in the evaporator is smaller than the output.

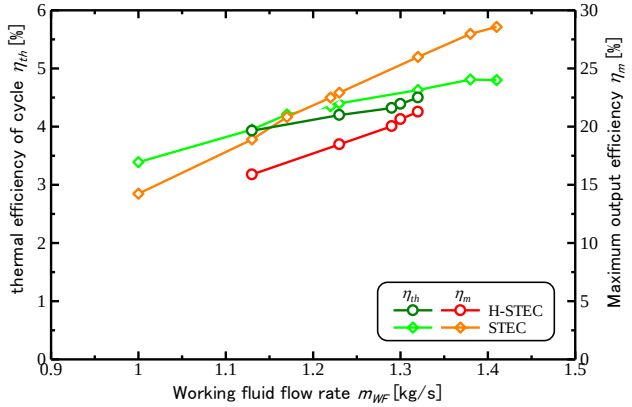

Fig.5 Cycle thermal efficiency and maximum power factor versus working fluid flow rate.

4. CONCLUSIONS

Parametric analysis was conducted to theoretically clarify the applicability of the green refrigerant R1224yd to replace R245fa and its effectiveness in comparison with STEC. As a result, it was theoretically clarified that the basic characteristics of R245fa and R1224yd in H-STEC are equivalent in performance for both working fluids. The applicability of R1224yd should be experimentally evaluated in the future.

The output of STEC and H-STEC were compared, and it was quantitatively clarified that the output of STEC was higher than that of H-STEC under the same analytical conditions. However, considering that the heat transfer performance of the STEC evaporator is reduced by the deposition of the hot spring water scale, there exists an inversion condition in which the output of H-STEC is higher than that of STEC. The chemical analysis was conducted to clarify the change of the hot spring water after the theory that the higher the heat passage coefficient, the more the stain causes the STEC output decrease and the more effective the H-STEC is, and the condensate showed that it was quantitatively clarified that the fouling components that cause scale were removed. In addition, a 30 kW H-STEC experiment was conducted in this study to investigate optimization parameters. As a result, it was experimentally clarified that the working fluid flow rate determines the turbine inlet superheat due to the constant hot spring steam temperature, and that there is an upper limit to the working fluid flow rate under the operating conditions of this H-STEC system. Therefore, the balance between the working fluid turbine inlet superheat and the hot spring steam temperature is important for the stabilization of this system.

NOMENCLATURE

A	Heat Transfer Area [m^2]
c_p	specific heat at constant pressure [kJ/(kg·K)]
s	specific entropy [kJ/(kg·K)]
h	specific enthalpy [kJ/kg]
L	latent heat [kJ/kg]
m	Mass, Volume Flow [kg/s] , [m^3/h]
Q	Heat exchange rate [kW]
$NETD$	Non-equilibrium temperature difference [K]
BPR	rise in boiling point [K]
DMS	demister loss [K]
T	Temperature [^{o}C], [K]
P	pressure [kPa]
ΔT_m	Logarithmic mean temperature difference [K]
ΔT_s	simple average temperature difference [K]
ΔT	Temperature drop [K]
U	Heat Passage Coefficient [kW/(m^2·K)]
W	output (e.g., of dynamo) [kW]
r_f	Feed water ratio [%]
R_W	dirt factor [(m^2·K)/W]
η	efficiency [%]
ρ	density [kg/m^3]
v	speed of moving fluid [m^2/s]
λ	Thermal conductivity [W/(m·K)]
δ	thickness [m]
M	Scale adhesion[g/m^2]

Reference

[1] Cabinet Office, Disaster Prevention Information Page, https://www.bousai.go.jp/

[2] Agency for Natural Resources and Energy, Ministry of Economy, Trade, and Industry, "Energy White Paper 2021", (2021)

[3] New Energy Foundation, "Proposal for the Promotion of Development and Utilization of Geothermal Energy". （2022）

[4] Organization for Promotion of Wide-Area Electricity Utilization, "Compilation of Supply Plan for FY2021". （2021）

[5] Motoaki Morita, Scale Problem in Hot Spring Binary Power Plants and Development of Inhibition Materials, Materia, Vol. 57, No. 10. （2018）